

XII. MOLECULAR APPLICATIONS

1. Limb Sounding Observations of the Earth’s Atmosphere

Thanks to it being our home, there is a long history of examining the atmosphere and surface of the Earth with observational geometries and tools that are not possible with other planets or astronomical objects. One of these tools greatly improves our understanding of the vertical distribution of various species in the Earth’s atmosphere – that of limb sounding. In this geometry, scans are taken across the limb of the earth with smallish telescopes in near-earth orbit at a variety of what are called tangent heights (or heights above the surface of the earth at the closest approach of the observing pencil beam). At near-IR wavelengths this requires a source, typically the sun, to be tracked; but at mid- to far-IR wavelengths (and beyond) collisions excite the molecules (just as in molecular clouds, as we will later see) and no background source is needed.

Thus, these long wavelength techniques work at all times, day or night. Figures 12.1 - 12.5 outline the technique of limb sounding at millimeter-wavelengths, and show some illustrative results. A major advantage of these long wavelength techniques is that they provide truly *global* coverage and complete sampling of diurnal variations (that is, variations from day to night, provided the appropriate orbits are used for the spacecraft). The down-side is the fairly large sampling size typically obtained, several hundred kilometers along the direction the observing path, as the imaging system cannot distinguish between different parcels of air along the same line-of-site. Thus, these results must be combined with smaller scale, *in situ* observations to gain a detailed understanding of the chemistry and dynamics of the earth’s atmosphere.

At millimeter-wavelengths, pressure broadening is quite important relative to doppler broadening, at least in the lowermost levels of the stratosphere, and this gives an additional handle on the vertical location of the emitting gas in addition to the various tangent heights used to reconstruct a vertical profile (that is, in a hydrostatic atmosphere, the width of a spectral feature is related to the height of the gas parcel that produces this feature, provided pressure broadening dominates the line shape function). The tangent heights are typically spaced by something like half the scale height of the atmosphere, which is 7 km for the Earth. Wind speeds are measured by the doppler shift of the narrow line cores, and so are best performed at altitudes where the pressure broadening is comparable to or less than the doppler widths.

In the infrared, doppler broadening typically dominates. While IR absorption measurements are typically tied to specific local times-of-day due to the observing geometry, and while they do not have the global coverage available to millimeter wave limb-sounding, they form an extremely powerful and important tool as Figures 12.6 and 12.7 attest. The ability to examine both polar and non-polar species is an extremely important capability, as pivotal greenhouse gases such as CO_2 and CH_4 cannot be studied at millimeter-wavelengths. In addition, the sensitivity is sufficiently high that a large number of isotopic species (Figure 12.6) and complex molecules (Figure 12.7) can be studied. In the latter case, it is the overall band profile that is used to recover the abundances, or mixing ratios, of species such as the chlorofluorocarbons (CFCs) or pivotal “reservoir” molecules like ClONO_2 whose fully rotationally resolved spectra result in features that are too weak for detection.

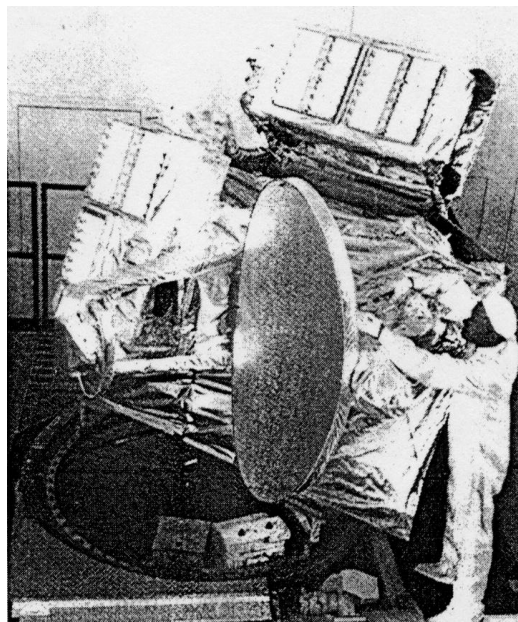
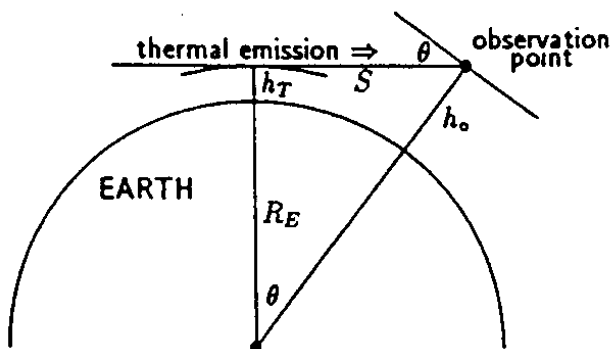


Figure 12.1– (Left) The observational geometry for millimeter-wave and infrared limb sounding observations of the Earth’s atmosphere. No background source is needed for the long wavelength studies, in the IR the Sun is typically used to collect spectra. (Right) The Upper Atmospheric Research Satellite Microwave Limb Sounder (UARS MLS) flight assembly. The vertical length of the antenna is 1.6 m.

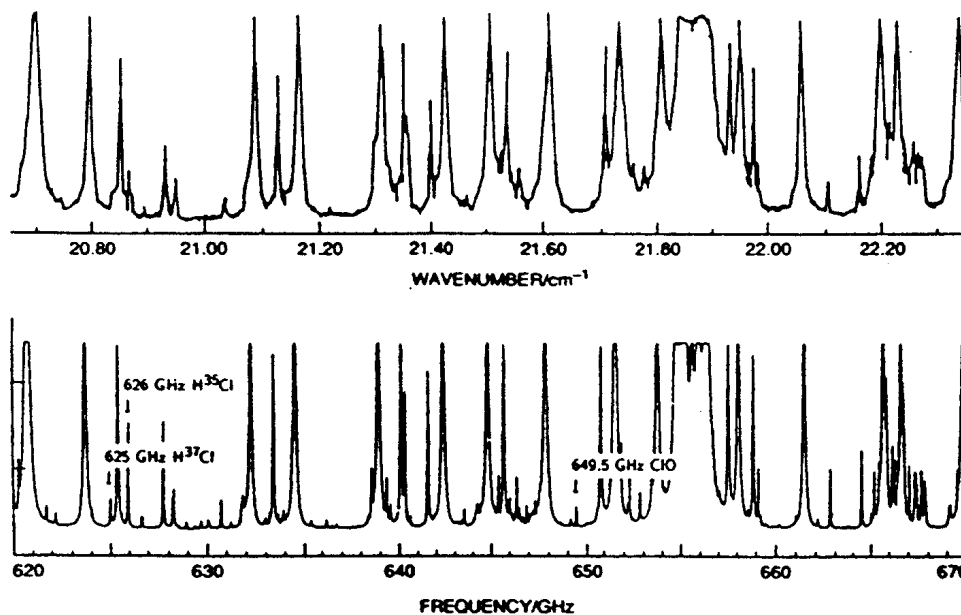


Figure 12.2– A portion of the stratospheric emission spectrum between 620-670 GHz. The observed spectrum is to the top, the bottom spectrum is a synthetic spectrum of the type that is used to fit the observed data.

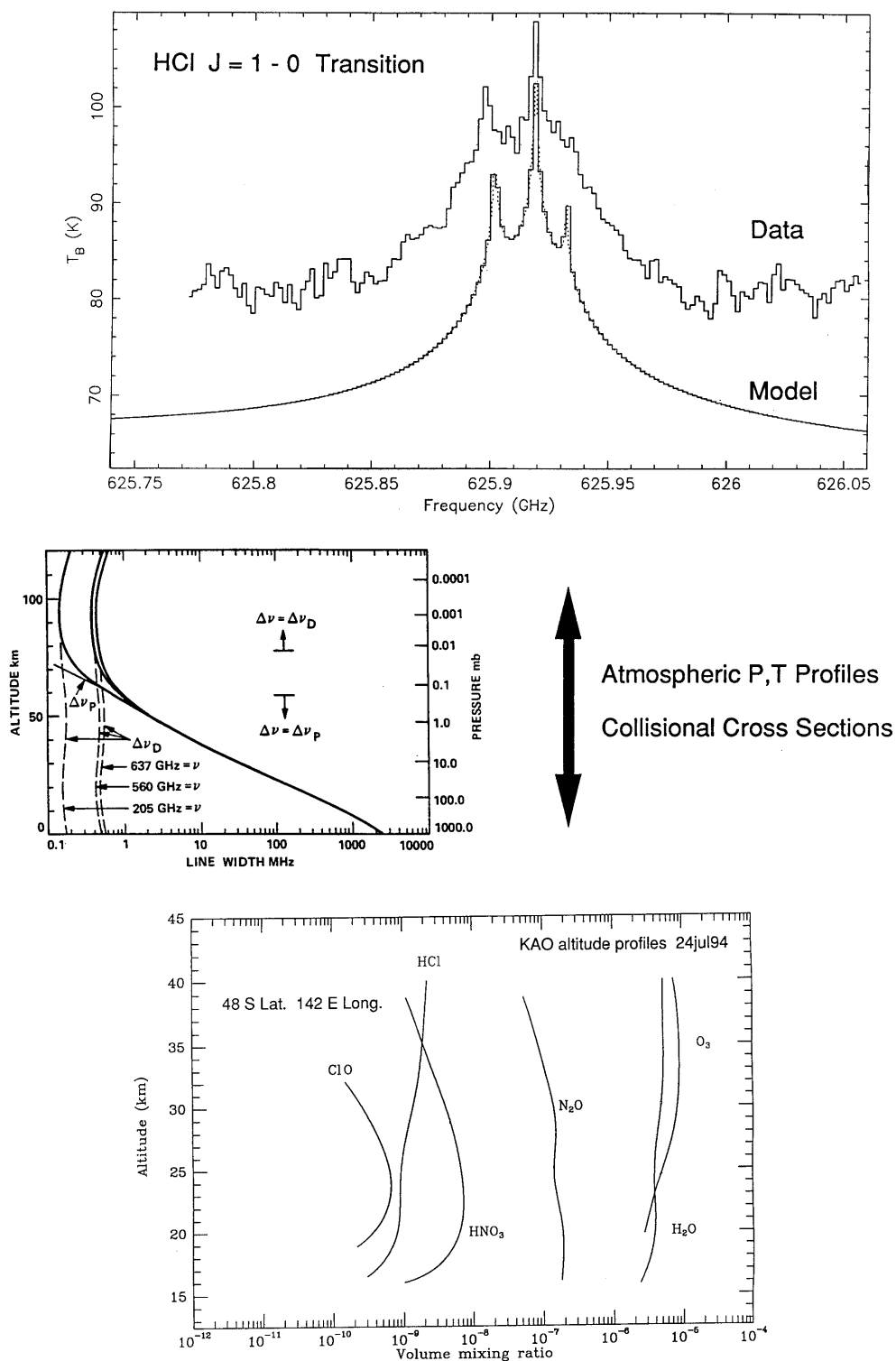


Figure 12.3– An illustration of the inversion procedures that convert the observed millimeter-wave limb sounding emission (top) into vertical mixing ratio profiles (bottom) via pressure broadening and scans of the tangent heights.

Figure 12.4– UARS MLS observations of the variation in ClO from 2-13 January 1992 toward the north pole. 60° north latitude is shown by the dotted circle, the ClO is in grey scale, and the 195 K level is the thin dashed line. The contour of constant vorticity is shown by the solid line.

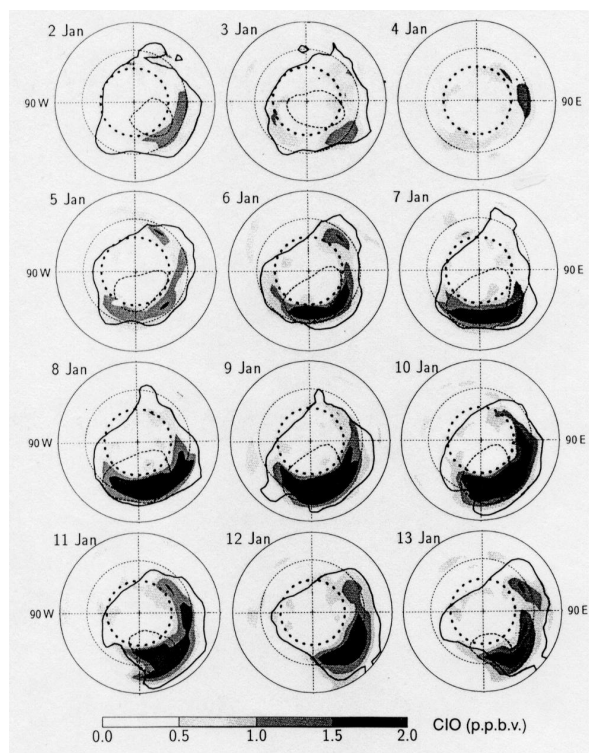
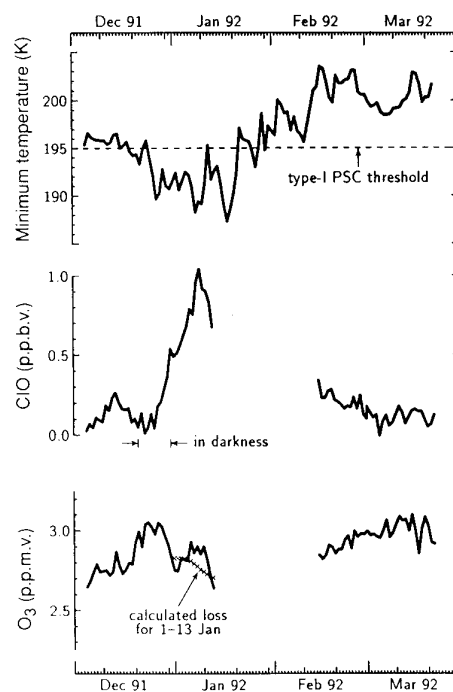


Figure 12.5– Temperature, ClO, and O₃ in the 1991-1992 northern hemisphere winter vortex for a lower stratospheric layer at 465 K potential temperature. The horizontal line indicates the approximate temperature below which nitric acid trihydrate PSCs form, and the activation of chlorine reservoir compounds is expected to begin.



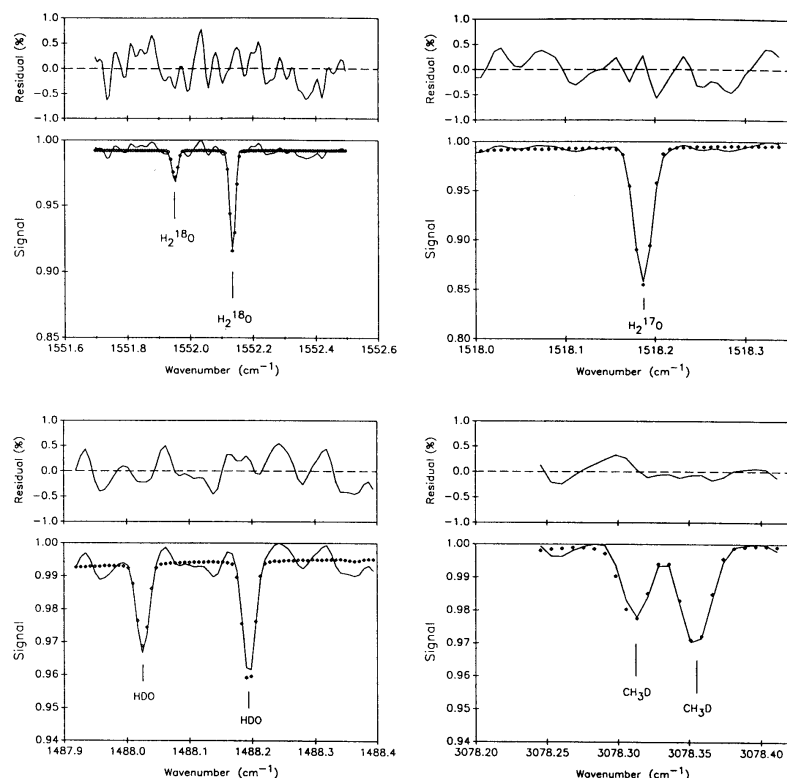
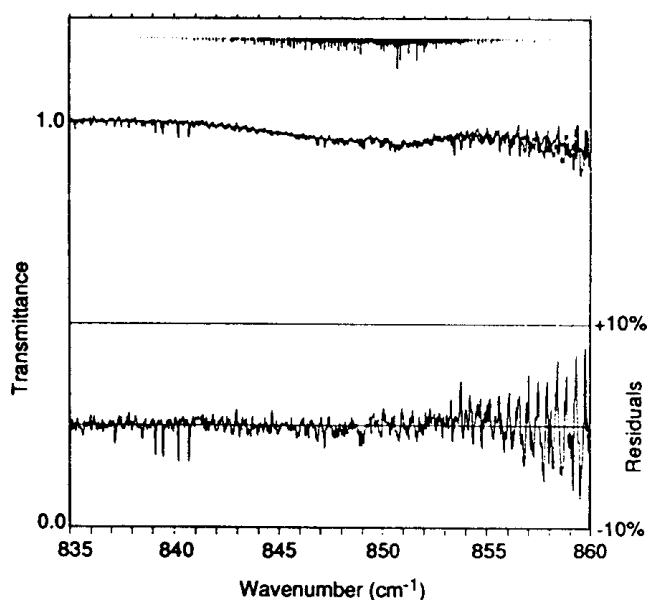


Figure 12.6– Examples of the ATMOS/Spacelab 3 and least squares best calculated fit (solid diamonds) for the infrared absorption limb sounding spectroscopy of isotopic water vapor and methane. The tangent heights and corresponding tangent pressures are 55.7 km and 0.42 mbar for H_2^{18}O ; 29.8 km and 12.4 mbar for H_2^{17}O and HDO. The CH_3D are for an extensive zonal average, the effective tangent height and corresponding tangent pressure 26.0 km and 21.8 mbar.

Figure 12.7– An example of a vibrational band fit, in this case to CFCl_3 . The structure at right arises from a HNO_3 band that is not modeled in this spectrum.



2. The Early Universe

(a) *Molecule Formation: $z \sim 1000-50$*

The formation of the Earth, the planets, the Sun, and all the other bodies in the Universe is of course one of the most intriguing questions man has posed himself. We will attempt here to outline for you, in a very sketchy way, the current “fairy tale” for the molecular chemistry of the early Universe. In the standard Big-Bang cosmology, the Universe was without any structure at the earliest time ($t < 10^{10}$ s). Its state could be characterized by a temperature $T = T_r$ (temperature of radiation) = T_m (temperature of matter), and a mean density n_H . It is well known from observations that the Universe expands. Remember that it is this, when coupled with the detection of the 2.7°K cosmic background radiation, that is the strongest direct evidence of the Big Bang hypothesis. By incorporating this expansion the standard theories predict that the temperature and density decrease with time as

$$T_r \propto (1 + z) \quad (12.1)$$

$$n_H \propto (1 + z)^3. \quad (12.2)$$

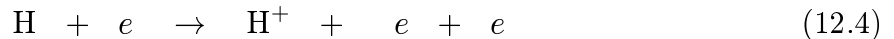
owing to the expansion. Here z is the **redshift**, which is defined such that the observed wavelength of a spectral line (say the $H\alpha$ line of atomic hydrogen) in a distant object is given by

$$\lambda_{obs} = (1 + z) \lambda_{rest}, \quad (12.3)$$

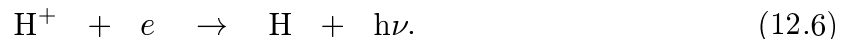
where λ_{rest} is the rest wavelength of the line. The redshift can be used either as a measure of distance from us, or the time since the beginning of the expansion. The present epoch is at $z = 0$, corresponding to a time some $t \sim 2 \times 10^{10}$ years after the beginning of the expansion.

In this early **radiation dominated** era, the temperatures are extremely high, as eq.(12.1) suggests. For example, at a time of some 10^{-4} s after the beginning of the expansion, the temperature has “dropped” all the way to 10^{12} K! At the very earliest times, matter and radiation are very strongly coupled. For example, at the temperatures at and before 10^{-4} s, the creation and annihilation of baryon-antibaryon pairs occurs (protons and neutrons are two of the less exotic members of the baryon family, baryon meaning “heavy one”). At somewhat lower temperatures (longer times), annihilation-creation rates drop and **nucleosynthesis** becomes important – but only for a short time. Indeed, the major part of Big Bang nucleosynthesis occurs during the first *three minutes* of the existence of the universe (as a very readable book with the title *The First Three Minutes* by S. Weinberg describes in much more detail).

Eventually, the temperature drops to the point at which the rates of ionization of H, e.g.



become small compared with the rates of recombination, e.g.



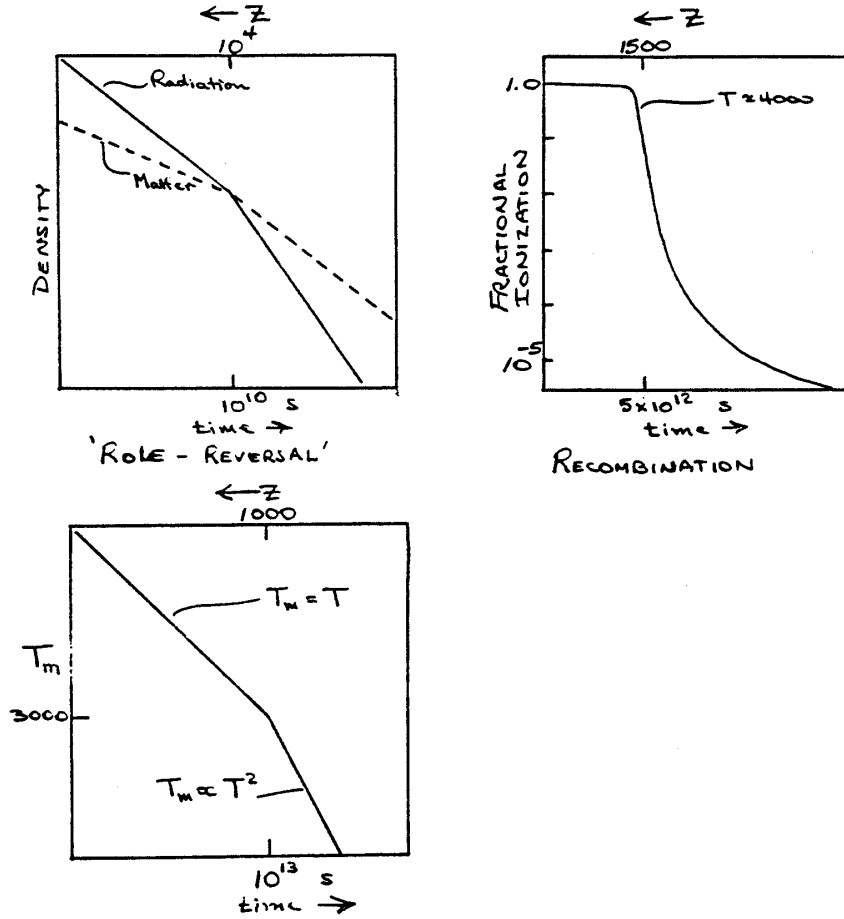


Figure 12.8– The “standard” model of the early universe.

As the universe cools, the matter changes from a state of an ionized plasma to a primarily neutral gas very rapidly. This **epoch of recombination** occurs at a temperature of about 7000-5000 K, when the universe was approximately 4×10^5 years old. He^{++} , He^+ , and H^+ recombine in the sequence of their decreasing ionization potentials. It is at this epoch, $z \sim 1500$, that the first chemical bond occurs. The gas consists of H, D, and Li nuclei created during the nuclear burning era with relative abundances of about $1:5 \times 10^{-5}:0.1:10^{-10}$ by number (recent observational studies of Be and B in very old stars may force a radical change in our thinking about early nucleosynthesis).

At approximately the same time, the matter becomes unable to interact strongly with the radiation any longer, and it evolves thermally independently of the radiation as time goes on, so that $T_m \neq T_r$ with

$$T_m \propto (1 + z)^2 \quad z \leq 1500. \quad (12.7)$$

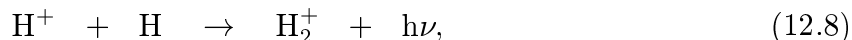
In this regime, the density of matter is higher than that of radiation, and the universe is said to be **matter dominated**; just as it is now. Here, a detailed statistical balance among various microscopic processes replaces thermodynamic equilibrium as the appropriate description of the state of matter. Eventually, the expansion will overcome

the recombination process (12.6) in controlling the decrease of the proton and electron densities, with the result that the ionization fraction will approach a non-zero, asymptotic value near $n(e)/n_H \sim 5 \times 10^{-5}$. Figure 12.8 presents a graphical depiction of how the various properties vary roughly with redshift (i.e. time).

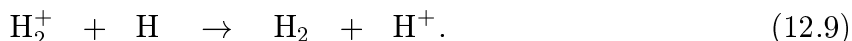
A number of detailed scenarios for primordial nucleosynthesis have now been worked out. Above 10^{11} K, equilibrium prevails and there is no need to keep track of prior history. Just below this temperature, a number of particles need to be kept track of (protons, electrons, photons, neutrinos, etc.). To calculate the production of various nuclei, the necessary input parameters include rates of nuclear reactions, time scale of the expansion, etc. Only very light nuclei are created in any abundance. Hydrogen is by far the most abundant element, with ^4He down by roughly a factor of ten in number (less in mass). Deuterium (D) and ^3He are down from H by nearly 10^{-5} , and ^7Li and ^7Be by nearly 10^{-10} . These models assume the early universe was not strongly “clumped.” If density variations are large, it is possible to synthesize larger amounts of elements in the Li – B range.

As many of you know, stars “burn” D and Li and do not make them; thus whatever we see now *must* be left over from the Big Bang. The oceans of the Earth, and our bodies as well, contain quite a reasonable amount of deuterium - atoms created in the very beginning of the universe some 10-20 billion years ago! Since no heavier, rock forming, elements were produced, the early universe was entirely gaseous.

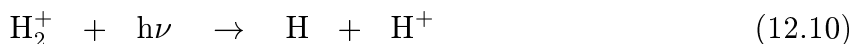
Because of the absence of dust in the early universe, molecules can only form by the process radiative association outlined earlier in these notes. However, because the allowed vibrational transitions of H_2 are exceedingly weak, the radiative association of $\text{H} + \text{H}$ to form H_2 is extremely slow. On the other hand, the few electrons and protons that are left after the recombination can act as “catalysts” to form molecules through the ionic radiative association of H^+ and H. That is,



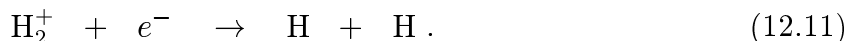
followed by *charge transfer* to form H_2 :



In the radiative association process, H and H^+ approach each other along the $2p \sigma_u$ repulsive curve (see Figure 11.2), so that the efficiency diminishes with decreasing temperature. The H_2^+ ions can be destroyed by photodissociation

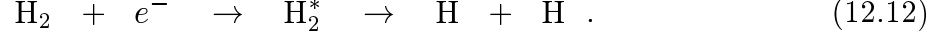


and dissociative recombination



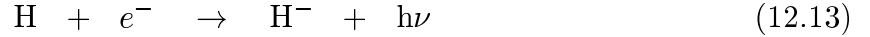
The threshold for H_2^+ photodissociation is 2.65 eV (c.f. Figure 11.2), so that the photodissociation rate diminishes very rapidly as the radiation temperature falls below 4000 K. Once this happens, charge transfer (equation 12.9) becomes the preferred reaction

of H_2^+ , and H_2 is formed efficiently. Note that a proton is returned upon the formation of H_2 , so that the sequence is catalytic. The principal destruction process of H_2 is the reverse of reaction (12.9), and electron-impact excitation leading to dissociation (remember the photodissociation cross section of H_2)

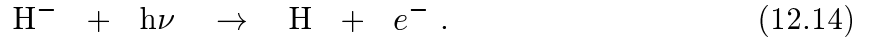


However, the processes are quite slow, so that most H_2 molecules survive. The H_2 formation rate is proportional to the density squared, which in turn, is proportional to $(1+z)^6$, so that there is only a short time in which the sequence can work efficiently. In fact, the formation of H_2 via these reactions ceases to be important at $z \sim 190$.

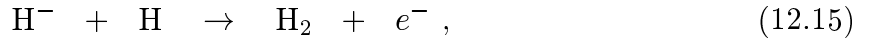
A second route to the formation of H_2 can occur at a later time, $z \sim 100$, where the negative ion H^- , formed by radiative attachment



is no longer destroyed by photodetachment



As we have seen in §VI, the process (12.14) has a threshold of 0.75 eV, or 16000 Å. Thus, the radiation temperature must fall below $T_r \sim 1000$ K before H^- is more rapidly destroyed by associative detachment



which leads to the formation of H_2 . This sequence is also catalytic since an electron is formed in reaction (12.15). Table 12.1 summarizes the rates for the various processes in the early Universe at different temperatures.

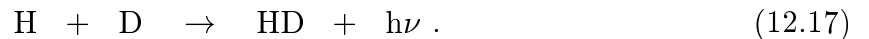
The H^- sequence ceases to be important at $z \sim 60$. The net result of both the H^+ and H^- sequences is that the matter ends up with a non-zero asymptotic molecular fraction as $z \rightarrow 0$, $f(\text{H}_2) \sim 10^{-6} - 10^{-5}$, depending on the density parameter Ω of the Universe. Figure 12.9 illustrates the abundances of H_2 as a function of redshift for a model with $\Omega=0.1$.

Small amounts of other molecules can be formed as well in this period. The first molecules formed were most likely He_2^+ and HeH^+ , initiated by radiative association of He with He^+ and H^+ . Their relative abundances are very low, however, as Figure 12.9 shows. HeH^+ can also be formed by reactions of H_2^+ ions in vibrational levels $v \geq 3$ with He:



The HeH^+ ions are mostly removed by the reverse of this reaction.

The HD molecule is formed and destroyed by reactions similar to those which control the abundance of H_2 . In addition, HD has a permanent dipole moment, and can be formed by radiative association



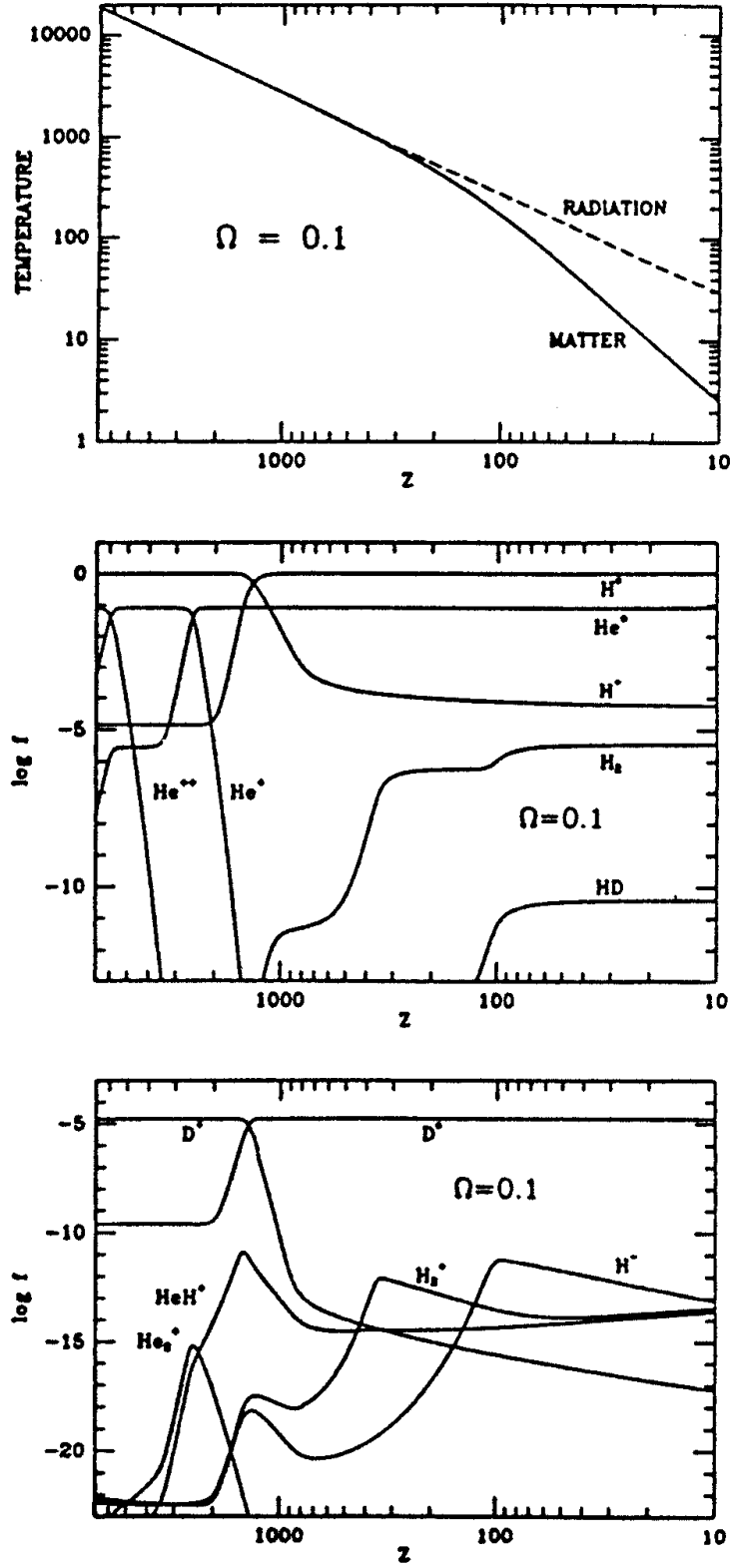
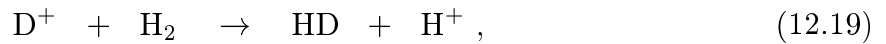


Figure 12.9– Thermal and chemical history of the Universe for a standard Big Bang model with $\Omega=0.1$ and $H_0=50 \text{ km s}^{-1} \text{ Mpc}^{-1}$ (from Latter 1989).

Table 12.1— Rates of Individual Processes as Functions of T

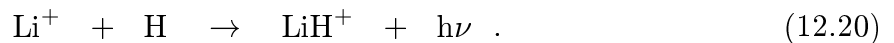
Z =	330	660	1300	
T =	1000	2000	4000	8000
$H + h\nu \rightarrow H^+ + e$	—	4.25 -27 s ⁻¹	1.15 -9	8.24 -1
$He + h\nu \rightarrow He^+ + e$	—	—	6.81 -23	4.24 -7
$H^+ + e \rightarrow H + h\nu$	1.43 -12 cm ² s ⁻¹	8.61 -13	5.20 -13	3.14 -13
$He^+ + e \rightarrow He + h\nu$	1.20 -12	7.67 -13	4.92 -13	3.15 -13
$H + e \rightarrow H^- + h\nu$	8.51 -16	1.41 -15	2.25 -15	3.23 -15
$H^- + h\nu \rightarrow H + e$	4.06 +1 s ⁻¹	1.52 +4	6.14 +5	7.47 +6
$H^- + H \rightarrow H_2 + e$	2.0 -9	2.0 -9	2.0 -9	2.0 -9
$H^- + H^+ \rightarrow H + H$	1.26 -7	8.94 -8	6.32 -8	4.47 -8
$H^+ + H \rightarrow H_2^+ + h\nu$	5.17 -18	1.89 -17	6.22 -17	1.67 -16
$H^+ + He \rightarrow HeH^+ + h\nu$	2.50 -19	9.21 -20	4.27 -20	2.21 -20
$H_2^+ + H \rightarrow H_2 + H^+$	6.4 -10	→	→	→
$H_2^+ + h\nu \rightarrow H^+ + H$	3.13 -15	1.08 -7	2.02 -2	9.85 +2
$H_2^+ + e \rightarrow H + H$	2.83 -8	2.19 -8	1.70 -8	1.31 -8
Cooling rates : [erg cm ⁻³ s ⁻¹]				
e - H	2.8 -70	1.40 -44	1.00 -31	2.7 -25
e - H ₂	1.06 -23	4.16 -23	2.22 -22	
H - H ₂	1.52 -25	2.23 -24	2.10 -23	8.93 -23

It can also be enhanced by the series of reactions



which is the same sequence that leads to HD in diffuse interstellar clouds. These two reactions can also lead to a substantial fractionation of HD in the early Universe.

Because of its much lower ionization potential, lithium remains ionized to a much lower radiation temperature than does hydrogen. Thus, the molecular ion LiH⁺ may be formed by the radiative association of Li⁺ and H, or



(b) *Molecules as Coolants: $z \sim 50$ -5*

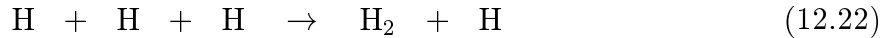
There are a number of other reaction sequences which can generate other molecules in the z range from 1000 - 100. At $z \sim 50$, the universe consists of an almost neutral atomic gas of hydrogen and helium with a fractional ionization of about 5×10^{-5} , a fractional molecular abundance of about 10^{-5} - 10^{-6} , and trace amounts of D, Li^+ , HD, HeH^+ , and LiH^+ .

The molecules are not mere curiosities, however, but can play an important role in the cooling of the gas at low temperatures in the range $T = 100$ - 1000 K, where the excited states of the atoms H and He are energetically inaccessible. At these temperatures, the vibration-rotation levels of H_2 can be collisionally excited. Subsequent radiative decay leads to cooling of the gas. Under some circumstances the less abundant molecules like HD, HeH^+ , and even LiH^+ can contribute significantly to the cooling, as Figure 12.10 shows. Figure 12.11 illustrates that the levels of the heavier molecules HD and LiH^+ lie at lower energies, so that they can be more effective at low temperatures. Also, their more probable dipole allowed radiative transitions partly compensate for their lower abundances.

Thus, molecules play an important role in the formation of the first protostars and protogalaxies in the early universe. These are thought to arise from initial anisotropies embedded in the universe, which can lead to collapsing pre-galactic clouds. Because of the molecules, the cooling is enhanced and the temperature lowered. This, in turn, lowers the characteristic value of the **Jeans mass**

$$M_J \sim T_m^{3/2} n_H^{-1/2} M_\odot, \quad (12.21)$$

which is the *smallest* mass for which gravitational contraction can overcome gas pressure. Thus, the fragmentation and contraction can occur on smaller, stellar mass scales owing to the presence of molecules. Once dense condensations arise, additional molecular processes will be important. In particular, the H_2 abundance in primordial protostars can be enhanced by *three-body association* reactions such as

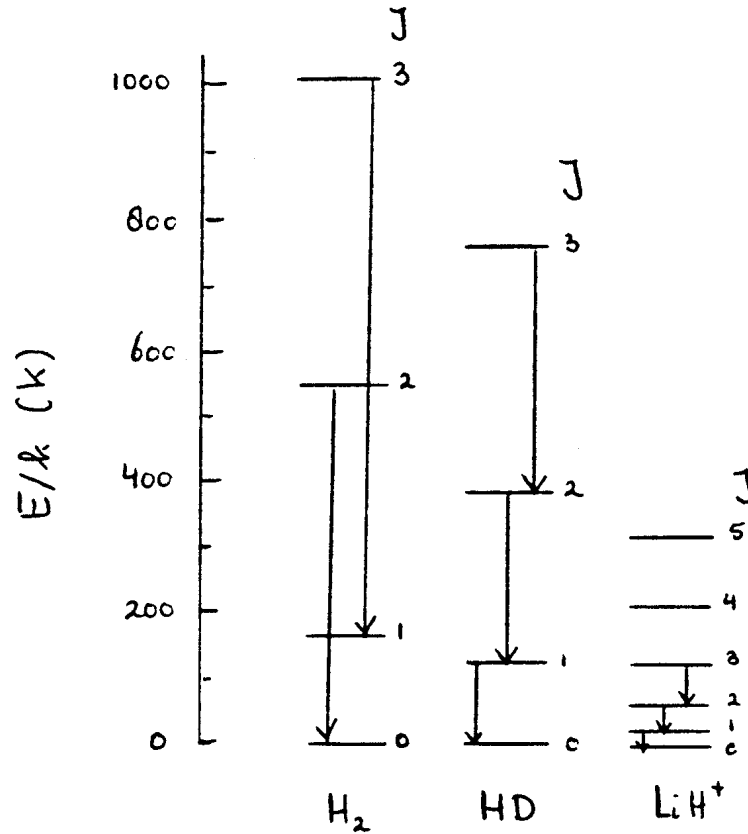
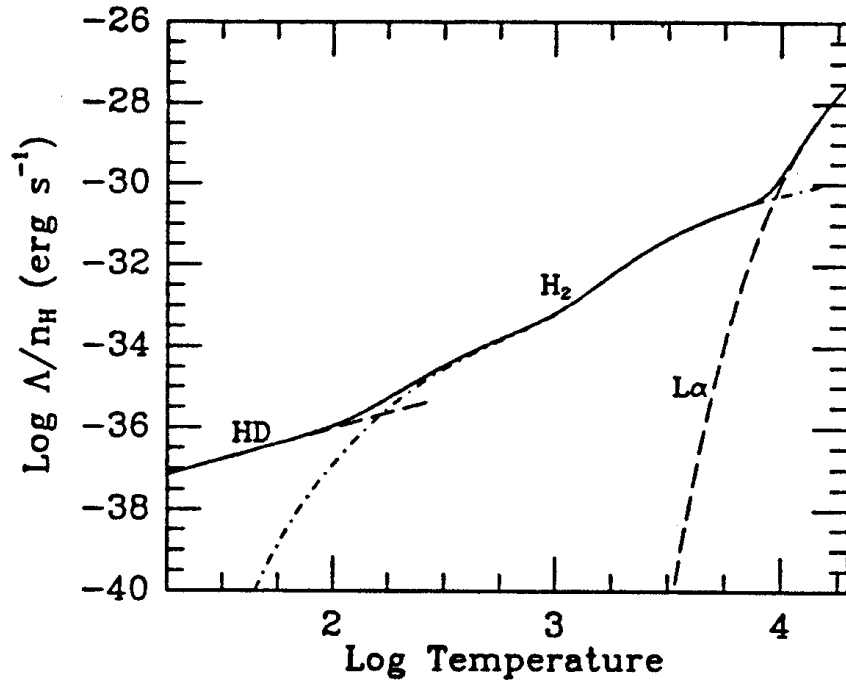


at densities above $n_{\text{H}} \geq 10^9 \text{ cm}^{-3}$, which plays a significant role in the subsequent evolution of these objects.

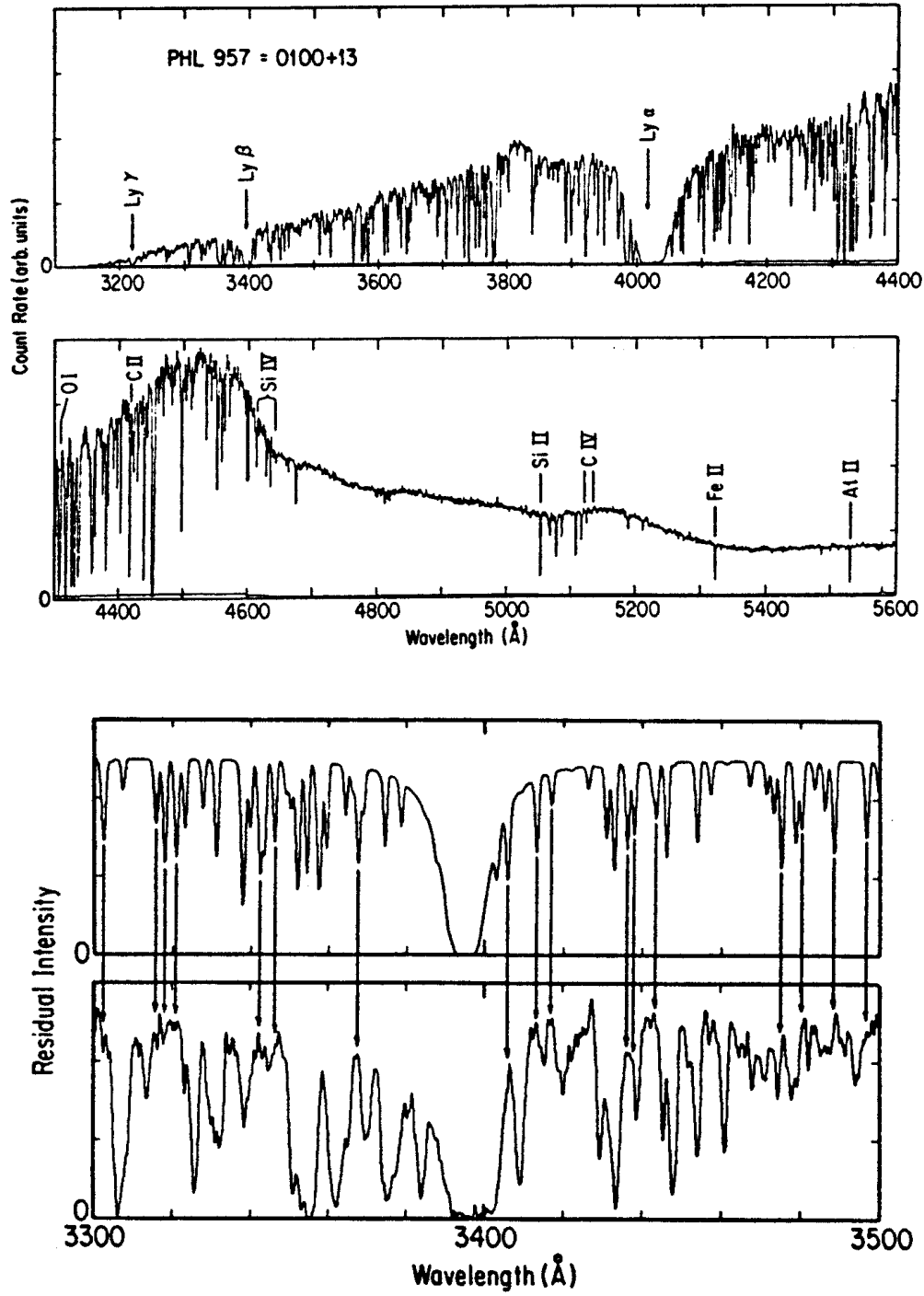
(c) **Optical Observations: $z \sim 5$ -0**

The molecules formed in the early Universe are likely to be destroyed by the ultraviolet photons and the hot gas that accompany the first generation of stars, so that they can no longer be observed. Nevertheless, they do affect the formation of the first stars, clusters and galaxies.

At somewhat more contemporary epochs, $z \sim 5$ -2, absorptions of stable molecules like H_2 and CO can be searched for in the spectra of high-redshift QSOs. While the violent environment of a QSO itself may be inhospitable to molecules, the light of the QSO has a non-zero probability of passing through a pregalactic cloud or a distant galaxy while traveling more than halfway across the Universe to reach us. Thus, this technique for observing is similar to that employed locally to study diffuse interstellar clouds.



Figures 12.10 and 12.11– (12.10) The variation with temperature of cooling rates due to H, H_2 , and HD (from Latter (1989)). (12.11) Energy level diagram for H_2 , HD, and LiH^+ illustrating why the molecules are effective coolants at different kinetic temperatures.



Figures 12.12 and 12.13– (12.12) A spectrum of PHL 957 obtained with the MMT at 1 Å resolution. The identified absorption lines arise in the predominant absorbing region at a redshift of $z=2.309$. The broad peak in the spectrum near $\lambda_{obs}=4500$ Å is the HI Lyman α of the QSO itself ($z \sim 2.69$), with the Lyman α forest lying to the blue. (12.13) Expanded view of Figure 12.12 over the range $3300 \leq \lambda \leq 3500$ (bottom). Top: Synthetic spectrum with anticoincidences marked.

Quite a number of attempts have been made to detect absorption lines of intergalactic H_2 in the spectra of QSOs. Remember that the lowest-lying absorption lines of H_2 correspond to the Lyman B $^1\Sigma_u^+ - X\ ^1\Sigma_g^+$ transitions at rest wavelengths $\lambda < 1100\ \text{\AA}$. At $z \geq 2$, these lines are shifted to wavelengths $\lambda > 3000\ \text{\AA}$, and thus become observable with ground-based telescopes. At the present time, it is possible to do absorption line spectroscopy on the brightest $z=2$ QSOs at a resolving power of $\lambda/\Delta\lambda \gtrsim 3 \times 10^4$ and with signal/noise ratios of $S/N \sim 100$ in reasonable integration times. However, these searches have not yet led to unambiguous identification of H_2 in the early Universe. The spectrum of PHL 957, a relatively bright, high-redshift QSO, illustrates the spectroscopic problem (see Figure 12.12). The redshift of the quasar is about 2.7, resulting in a Lyman α **emission** peak at about $4500\ \text{\AA}$. However, at shorter wavelengths, a large number of absorption lines are seen, which form the so-called *Lyman α forest*. These are all H I Lyman α lines at smaller redshifts due to material along the line of sight to the QSO.

One system at $z=2.309$ has a particularly large atomic hydrogen column density, $N(\text{H}) = 2.5 \times 10^{21}\ \text{cm}^{-2}$, resulting in strong, damped, H I Lyman lines. In clouds with such large column densities in our own Galaxy, H_2 is present in nearly equal amounts. However, searches for H_2 lines are complicated by the fact that these lines also fall shortward of H Lyman α , so that there is severe confusion between the expected lines of H_2 at $z = 2.309$ and the plethora of H I Lyman lines at other redshifts. PHL 957 has been regarded as one of the best candidates for the identification of H_2 ; however, detailed comparisons of the spectra in Figure 12.5 with simulated H_2 spectra for a variety of excitation conditions demonstrates that H_2 is not present (see Figure 12.13). The upper limit on the molecular fraction at $z = 2.309$ is quite low, $f(\text{H}_2) = N(\text{H}_2)/N(\text{H}) < 2 \times 10^{-6}$, in comparison with that in Galactic interstellar clouds of comparable column density of H, where $f(\text{H}_2) \sim 1$. The most likely explanation for this is an intense, “hard” dissociating flux due to the background QSOs.

More recently, spectra have been obtained of the QSO PkS 0528-250 that are consistent with the identification of H_2 lines at $z = 2.811$, where $N(\text{H}) = 1.3 \times 10^{21}\ \text{cm}^{-2}$. Figure 12.14 shows the observed spectrum, which can be compared in detail with a theoretical H_2 spectrum for $T_{ex} \sim 100\ \text{K}$ and $N(\text{H}_2) = 10^{18}\ \text{cm}^{-2}$. The most remarkable aspect of the comparison is that no **anti-coincidences** are found, so that this amount of H_2 could indeed be present in the cloud. The implied molecular fraction, $f(\text{H}_2) \sim 10^{-3}$, appears too large to result only from the gas-phase processes described in Section (a). If H_2 forms on the surfaces of dust present in this system, then it may be possible to estimate the dust content of the absorbing region.

Note that at $z = 2.811$, the H_2 molecules absorb the QSO light at a time near 87% of the age of the Universe into the past, if a low-density cosmology like that of Figure 12.9 applies. Such observations probe conditions over time intervals that are long compared with the lifetimes of stars that enrich the Universe in heavy elements via nucleosynthesis. In this way, the chemical evolution of the cosmos can be probed directly. Table 12.2 summarizes the derived abundances in a number of clouds at large z and in a galactic cloud, $\zeta\ \text{Oph}$, with similar properties.

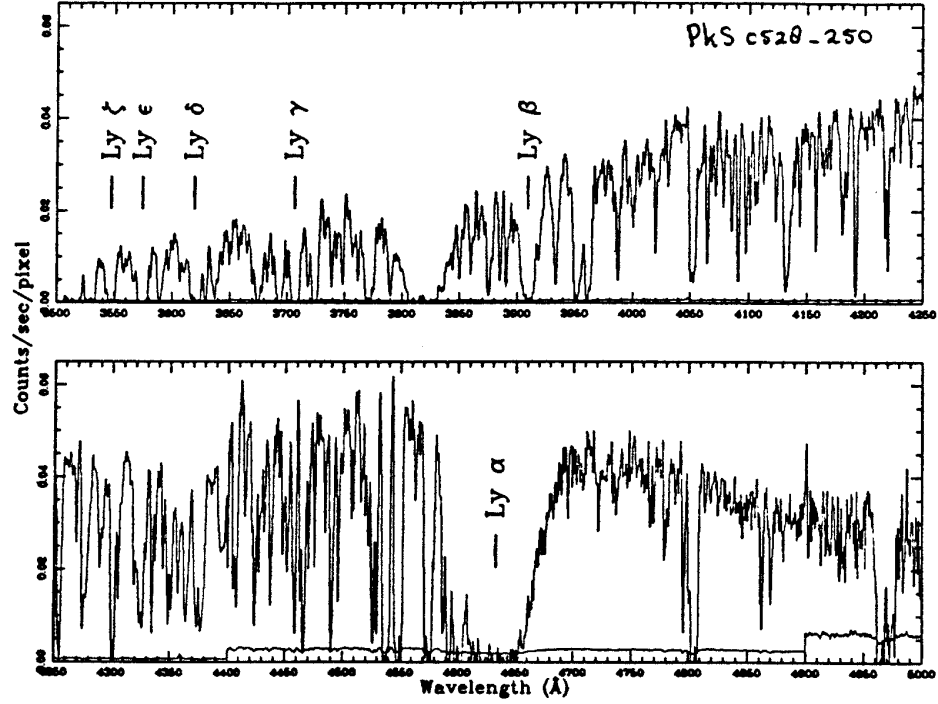


Figure 12.14– Composite of all of the 1 Å resolution data of PKS 0528-250. The positions of the Lyman absorption lines in the $z=2.8110$ system are marked. The intensity scale has not been corrected for atmospheric extinction or λ -dependent sensitivity of the instrument.

Table 12.2– Properties of High- z Clouds and a Galactic Cloud

	Cloud:	MC 1331+170	PHL 957	PKS 0528-250	ζ Oph
Property					
z		1.776	2.309	2.811	0
$N(\text{H})$	(cm^{-2})	1.5×10^{21}	2.5×10^{21}	1.3×10^{21}	5.2×10^{20}
$N(\text{H}_2)$	(cm^{-2})	...	$< 5 \times 10^{15}$	10^{18}	4.2×10^{20}
$N(\text{C}^+)$	(cm^{-2})	5.9×10^{16}	7.8×10^{15}	...	9.3×10^{16}
$N(\text{CO})$	(cm^{-2})	$< 1.1 \times 10^{13}$	$< 4 \times 10^{13}$	$< 5 \times 10^{15}$	2.0×10^{15}
$[\text{C}]/[\text{H}]$		$(0.3 - 4) \times 10^{-4}$	4×10^{-6}	...	3×10^{-4}

References

- Black, J.H. 1990, in *Molecular Astrophysics*
 Black, Chaffee, and Foltz 1987, *Ap. J.* **317**, 442.
 Dalgarno and Lepp 1987, in *Astrochemistry*, IAU Symposium 120.
 Foltz, Chaffee and Black 1988, *Ap. J.* **324**, 267.
 Latter, W. 1989, Ph.D. Thesis, University of Arizona.

(d) Millimeter-wave Observations: $z \sim 5-0$

The early Universe is particularly accessible to observations in the millimeter and submillimeter wavebands. Whereas the broadband flux from distant galaxies is diminished in the UV and optical both due to the redshift and obscuration by internal dust, the same dust produces a large peak in the rest-frame far-infrared, which, when redshifted, greatly enhances the millimeter and submillimeter emission from these objects. This general behavior is illustrated quantitatively for the spectral energy distribution of a bright starburst galaxy in Figure 12.15, and is called “the negative K-correction” by astronomers. This K -correction overcomes the effect of the inverse square law and cosmological surface brightness dimming, so that the flux density measured in the submillimeter waveband is almost independent of redshift from redshifts of about 0.5 to greater than 10! This gives an enormous advantage to observations at submillimeter wavelengths, where deep surveys are dominated by galaxies at the highest redshifts.

Indeed, some of the highest redshift objects known today are very luminous sources at millimeter wavelengths. The discovery of CO in the $z = 2.3$ galaxy IRAS F10214+4724 dramatically opened up the distant Universe to millimeter and submillimeter astronomy. Since then CO has been detected in several other high redshift objects. The most remarkable discovery is that large amounts of dust and CO molecules are present already at $z = 4.7$, in the object BR 1202-0725, the image of which is shown in Figure 12.16. This redshift corresponds to a look-back time of 92% of the age of the Universe, showing that enrichment of the interstellar medium occurred at very early epochs.

In addition to the negative K-correction, there is another factor which can enhance the flux of distant objects at all wavelengths, namely the phenomenon of gravitational lensing. The gravitational fields of foreground galaxies, clusters and large-scale structure in the Universe deflect light rays, and so distort the appearance of the background sky. Close to massive objects, the deflection can generate highly magnified multiple images of background galaxies. This is called strong lensing, and the magnification factors can easily exceed ten. Weak lensing is also ubiquitous, here the shapes of background galaxies are subtly and systematically sheared with negligible magnification. By observing the relative positions and magnifications of images produced by a lens it is possible both to study background galaxies that would be too faint to detect without the gravitational magnification, and to impose tight constraints on the gravitational potential of the foreground lens. Due to sensitivity limitations of current (sub)millimeter-wave telescopes and arrays, the high redshift galaxies presently known are almost all assuredly lenses, even those that appear as single sources.

The main reason for studying the detailed properties of molecular gas at high redshifts is that the composition of the molecular gas and its physical conditions are important for understanding the star formation processes. The assumption of a universal initial mass function (that is, the assumption that a given range and frequency of stellar masses are obtained from the collapse of molecular clouds), for instance, can only be tested by a detailed comparison of the properties of molecular gas in distant galaxies with that of our own Galaxy. The chemical evolution as a function of redshift is important for understanding the evolution of galaxies as a whole and the star formation activity during different epochs of the Universe. Another important reason is that molecular absorption

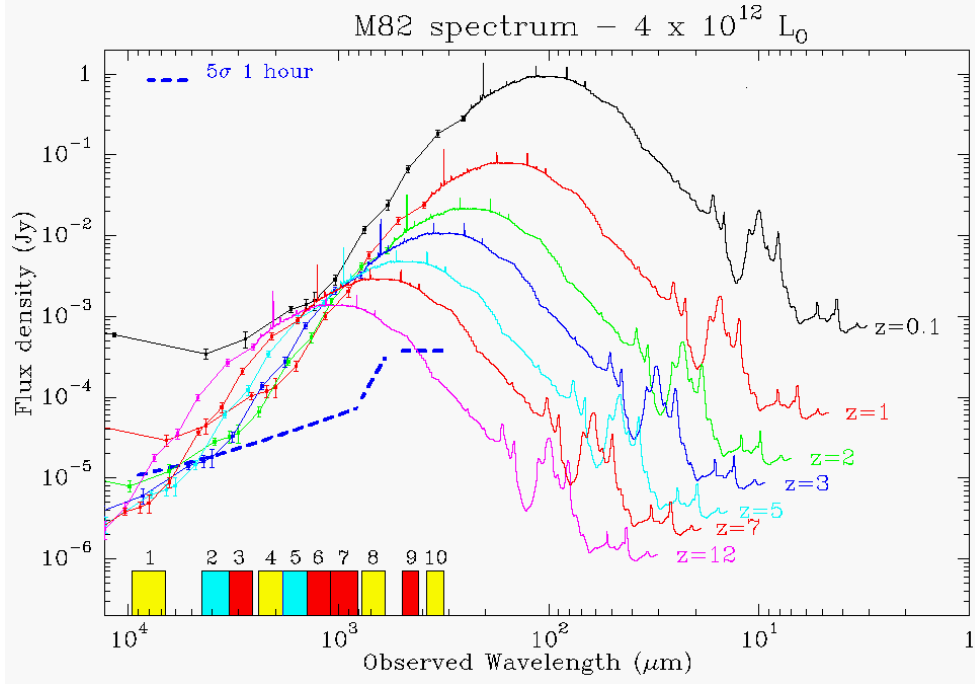


Figure 12.15– Observer-frame spectrum of a $4 \times 10^{12} L_{\odot}$ galaxy with increasing redshift from $z = 0.1$ to 12. The figure is based on the spectrum of the nearby starburst galaxy M82, including all available infrared, radio, and submillimeter data, and assumes a cosmology with $H_0 = 50 \text{ km s}^{-1} \text{ Mpc}^{-1}$, $\Omega_0 = 0.3$ and $\Omega_{\lambda} = 0.7$.

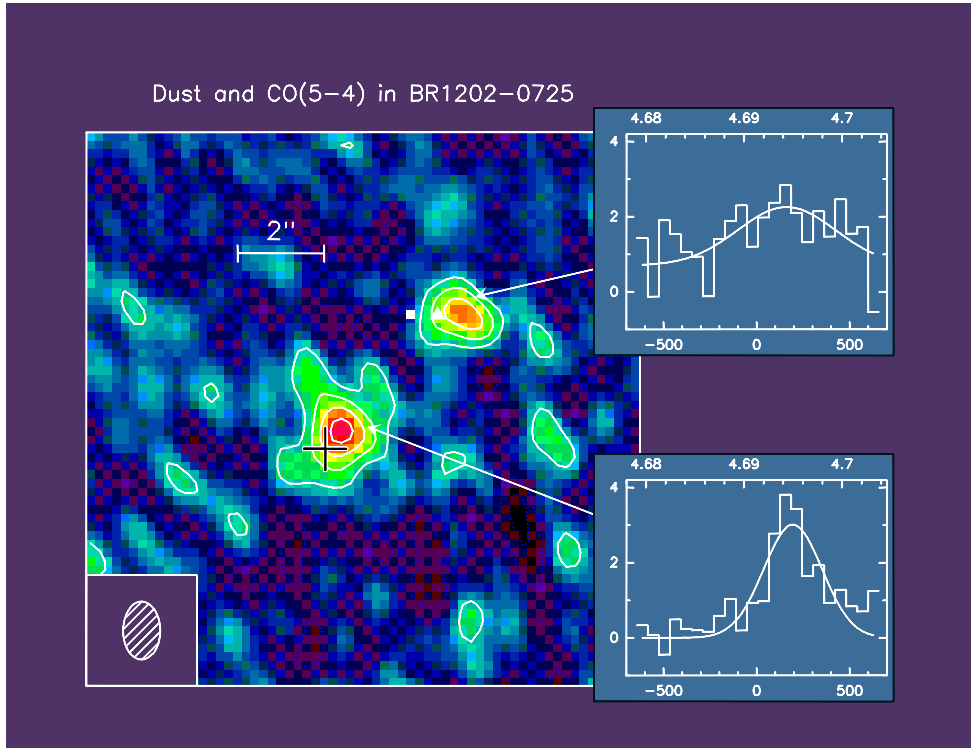


Figure 12.16– The quasar BR1202-07 at $z = 4.69$, mapped in the dust continuum at 1.3 mm with the IRAM interferometer. The insets show the CO (5-4) spectra of each component, which arise from the gravitational lens formed by a foreground galaxy.

lines allow a measure of the temperature of the cosmic microwave background (CMB) as a function of redshift. The energy levels of the lower transitions of many common molecules are in the range 4-10 K. At redshifts $z > 0.5$, these transitions will be radiatively coupled to the CMB radiation field. At $z \geq 2$ the CMB is likely to dominate the excitation. Molecular absorption lines are therefore excellent thermometers of the temperature of the CMB.

To acquire detailed knowledge about the physical and chemical properties of the molecular gas in distant galaxies, observations of rare but diagnostically important molecules are needed. These lines are weak, but can be accessible when seen in absorption against a continuum background source. In contrast to the strengths of emission lines, which decrease with distance, the depths of absorption lines are, to first order, independent of distance. This has previously enabled optical astronomers to gain detailed information about the atomic gas in galactic halos of high redshift galaxies and to study the intergalactic medium, using high redshift quasars (QSOs) as background continuum sources, as outlined above. The same principle holds true for molecular absorption lines, but only a few systems have been studied to date due to sensitivity limitations.

The utility of molecular absorption lines for obtaining detailed information about molecular gas in distant galaxies has been demonstrated, however, through the detection of four such absorption systems at redshifts ranging between $z = 0.25 - 0.89$. In these systems more than thirty different transitions, from 18 different molecules have been detected. Examples are shown in Figure 12.17. Most of the molecules have been observed in two or more transitions, allowing a direct derivation of physical properties. In addition five different isotopic variants have been detected: ^{13}CO , C^{18}O , H^{13}CO^+ , HC^{18}O^+ and H^{13}CN ; enabling initial assessments of the nucleosynthetic history of the gas to be undertaken.

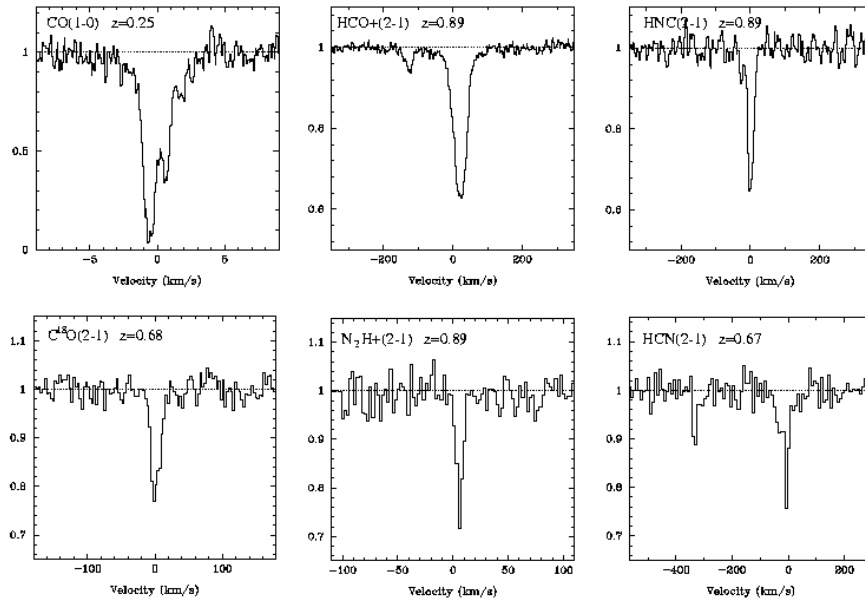


Figure 12.17– A set of millimeter absorption lines observed along the line of sight towards the quasar PKS 1830-211 using the IRAM 30m telescope. The molecular absorption occur at various intermediate redshifts which are given in each panel with the line identification.

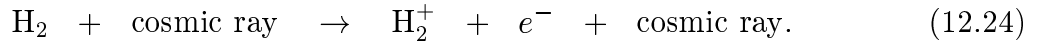
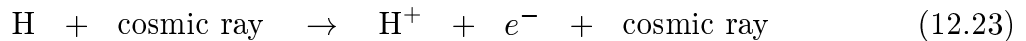
3. Molecular Clouds

The chemistry in interstellar molecular clouds is a vast subject, which, due to lack of time, will not be discussed extensively here (much like the other examples!). More details of the chemistry which occurs in these objects can be found in Ge/Ch 128. The atomic and molecular processes important in interstellar chemistry have already been outlined in § XI, and interstellar chemistry consists mostly of determining systematically for each species what the dominant formation and destruction processes are. This, of course, depends on the characteristics of the region, such as temperature, density, strength of the incident radiation field, and the elemental abundances. We will illustrate this with a few examples, and will concentrate on gas phase processes and observations. Studies of the condensed phase are best carried out using infrared spectroscopy of grains and their mantles, as illustrated in Figures 9.33-9.36.

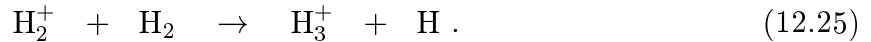
(a) Diffuse Interstellar Clouds

Diffuse interstellar clouds are the tenuous clouds with visual extinctions less than about one magnitude. As we have seen before (§ VI.2, § X.3b), these clouds can be observed by the absorptions of the atoms and molecules in the clouds superposed on the spectra of bright background stars. Diffuse clouds have temperatures and densities in the range of $T \sim 20\text{-}100$ K and $n_{\text{H}} \sim 20\text{-}200 \text{ cm}^{-3}$. Only the simplest diatomic molecules are found in these clouds: H_2 , HD, CH, CH^+ , C_2 , CN, CO, and OH. Many other molecules, such as H_2O , C_3 , HCl, MgH, ..., have been searched for without success, although H_3^+ has recently been detected. Because they are transparent, the ultraviolet radiation from the background interstellar field (§ XI.1d) rapidly destroys the molecules by photodissociation, thus preventing the build-up of larger species.

Let us look as an example at the oxygen chemistry in diffuse clouds, for which the network is illustrated in Figure 12.18. Atomic oxygen has an ionization potential slightly higher than 13.6 eV, so that O cannot be directly photoionized by the interstellar radiation field. Oxygen is therefore mostly neutral in interstellar clouds. The source of ionization which drives the ion-molecule chemistry comes in this case from the cosmic rays interacting with H and H_2 , or



The production of H_2^+ is followed by the rapid reaction with H_2 leading to H_3^+ :



The cosmic rays are high energy nuclei which are ubiquitous in the Galaxy, and which can even penetrate dense interstellar clouds. The rate at which they ionize atomic hydrogen is denoted by ζ [s^{-1}]. Estimates of the cosmic ray ionization rate range from $\zeta \sim 10^{-17}\text{-}10^{-16} \text{ s}^{-1}$, which is small compared with typical photoionization rates in the unattenuated interstellar radiation field of $10^{-10}\text{-}10^{-9} \text{ s}^{-1}$. However, in the absence of any photoprocesses, as in the case of oxygen, the cosmic rays can provide the small fraction of reactive H^+ and H_3^+ ions necessary to initiate the ion-molecule chemistry.

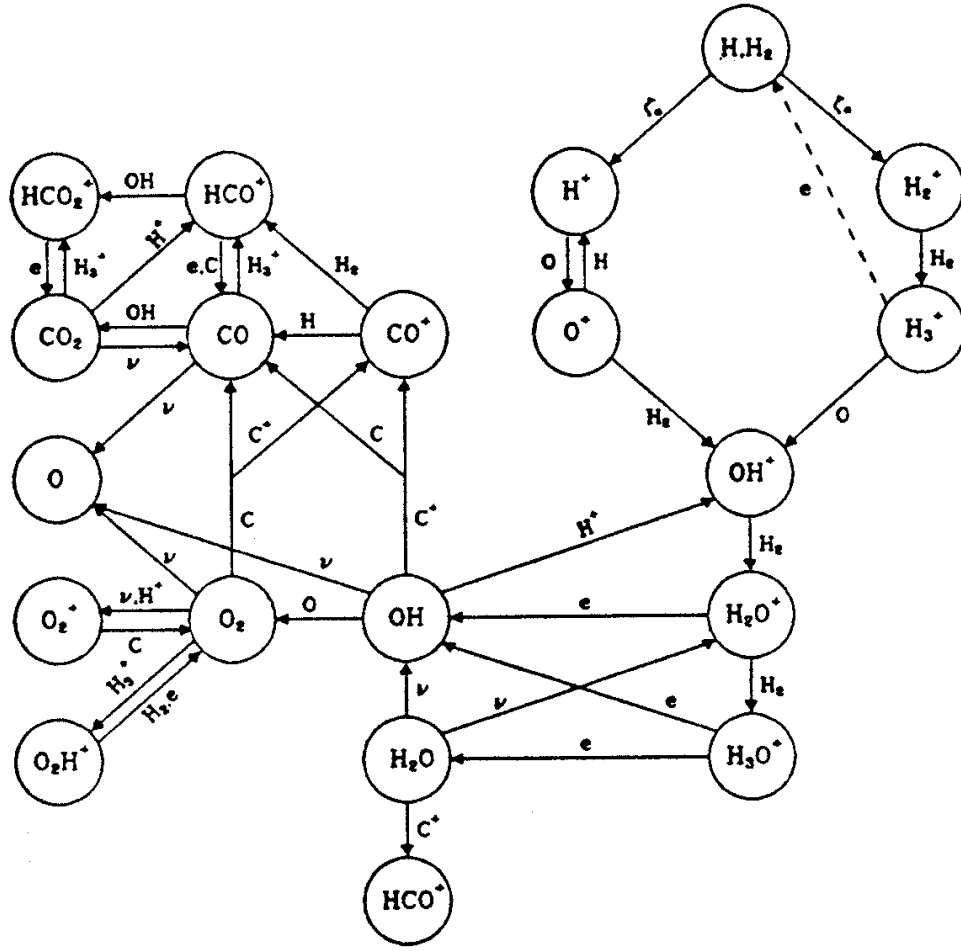


Figure 12.18– Oxygen chemistry in interstellar clouds.

We have seen in § V.6 that the ionization potential of O is accidentally very close to that of H, so that the near-resonant charge transfer process



can occur rapidly at low temperatures. Once a small amount of O^+ is formed, it reacts rapidly with H_2 to form OH^+ , essentially on every collision. Alternatively, OH^+ can be formed by the reaction of H_3^+ with O. The rest of the oxygen network consists of reactions with H_2 until an ion is formed – H_3O^+ in this case – for which the subsequent reaction with H_2 is endothermic. The ions then dissociatively recombine to form OH and H_2O , with relative amounts determined by the branching ratios. This “end-of-the-food-chain” sequence followed by dissociative recombination forms the backbone of the chemistry in interstellar clouds. Subsequent reactions of the OH and H_2O with C^+ , formed by the photoionization of C, lead to the formation of CO. A very thorough discussion of the chemistry in diffuse interstellar clouds may be found in van Dishoeck and Black (1988, in *Rate Coefficients in Astrochemistry*).

(b) Dense Interstellar Clouds

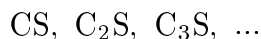
(i) Observations

In dense or dark interstellar clouds, the temperatures are typically $T \sim 10\text{--}50$ K, and the densities lie between $n_{\text{H}} = 10^4\text{--}10^7 \text{ cm}^{-3}$. At such low temperatures, only the rotational energy level spacings of molecules are comparable to kT . Thus, in general only rotational transitions between the lowest few J levels can be observed in dense interstellar clouds, which occur at millimeter and submillimeter wavelengths. For example, we have seen that for the abundant CO molecule, the maximum population occurs in the $J = 1$ level at 10 K, and $J = 4$ at $T = 100$ K. Thus, the $J=1 \rightarrow 0$ CO line at 2.6 mm (115 GHz) and the $2 \rightarrow 1$ line at 1.3 mm (230 GHz) are usually the strongest lines in dense interstellar clouds. Because H_2 itself is not directly observable, the CO emission is used as a *tracer* of the amount of molecular material in an interstellar cloud.

Since the dense clouds are opaque, absorption line studies of electronic transitions, such as those used to study diffuse clouds, are not possible. Occasionally, however, embedded infrared sources can be used to search for molecules by their vibration-rotation absorption lines at infrared wavelengths, as we have outlined previously.

More than one hundred different interstellar molecules have been detected to date in interstellar clouds, not including simple isotopic variants. Table 12.3 is the complete list as of several years ago, an up to date list may be found at <http://www.cv.nrao.edu/~awootten/allmols.html>. Most of these detections indeed result from searches at millimeter wavelengths. It is seen that the majority of the molecules are organic species, i.e. they contain predominantly carbon. Less than one-quarter of the detected molecules are inorganic species, such as SO, SiO, and NH_3 . Several abundant interstellar molecules were detected in interstellar space before they were synthesized in a laboratory on Earth. Famous examples include HCO^+ (“X-ogen”), N_2H^+ (“Y-ogen”) and C_3H_2 . The wide range of species and the nature of the rotational modes of asymmetric tops leads to a very dense spectrum, as the summary of the Orion molecular cloud emission in the introductory notes to this course shows.

Some curiosities to ponder: Several series of long chain molecules have been detected, e.g.



The largest molecule detected to date is HC_{11}N , containing 13 atoms. In contrast to the long carbon chains, only one ring molecule has been detected to date in interstellar clouds: C_3H_2 , whose spectrum was illustrated in Figure 8.19. In circumstellar envelopes, cyclic SiC_2 has been observed as well.

(ii) Molecular Excitation and Radio Line Formation

In order to understand better how chemical abundances are derived from spectra, it is useful to make a few remarks about molecular excitation and radio line formation in

TABLE 12.3 IDENTIFIED INTERSTELLAR AND CIRCUMSTELLAR MOLECULES^a

Species	Name	Species	Name	Species	Name
H ₂	molecular hydrogen	C ₂ H ₂	acetylene	C ₃ H	vinyl cyanide
C ₂	diatomic carbon	C ₃ H	propynylidyne (<i>l</i> and <i>c</i>)	CH ₂ CHCN	methylacetylene
CH	methylidyne	H ₂ CO	formaldehyde	CH ₃ C ₂ H	acetaldehyde
CH ⁺	methylidyne ion	NH ₃	ammonia	CH ₃ CHO	methylamine
CN	cyanogen	HNCO	isocyanic acid	CH ₃ NH ₂	cyanodiacyetylene
CO	carbon monoxide	HOCO ⁺	protonated carbon dioxide	HC ₃ N	
CS	carbon monosulfide	HCNH ⁺	protonated hydrogen cyanide		
OH	hydroxyl	HNCS	isothiocyanic acid		
HCl	hydrogen chloride	C ₃ N	cyaethynyl	HCOOCH ₃	methyl formate
NO	nitric oxide	C ₃ O	tricarbon monoxide	CH ₃ C ₃ N	methylcyanoacetylene
NS	nitrogen sulfide	H ₂ CS	thioformaldehyde	CH ₃ C ₄ H	methyldiacetylene
SiC	silicon carbide*	H ₃ O ⁺	hydronium ion	CH ₃ CH ₃ O	dimethyl ether
SiO	silicon monoxide	C ₃ S		CH ₃ CH ₂ CN	ethyl cyanide
SiS	silicon sulfide			CH ₃ CH ₂ OH	ethanol
SO	sulfur monoxide			HC ₇ N	cyanohexatriyne
PN					
CP	*				
SO ⁺	sulfoxide ion	C ₄ H	butadiynyl		
NaCl	sodium chloride*	C ₃ H ₂	cyclopropenylidene	CH ₃ C ₄ CN	acetone †
AlCl	aluminum chloride*	H ₂ CCC	propadienylidene	CH ₃ CH ₃ CO	
KCl	potassium chloride*	HCOOH	formic acid		
AlF	aluminum fluoride* †	CH ₂ CO	ketene	HC ₉ N	cyano-octa-tetra-yne
		HC ₃ N	cyanoacetylene	HC ₁₁ N	cyano-deca-penta-yne
		CH ₂ CN	cyanomethyl		
		NH ₂ CN	cyanamide		
		CH ₂ NH	methanimine		
		CH ₄	methane		
		SiH ₄	silane*		
		C ₄ Si	*		
		C ₅	pentatomic carbon*		
		HCCNC	isocyanoacetylene		
C ₂ H	ethynyl				
CH ₂	methylene †	C ₅ H	pentynylidyne		
HCN	hydrogen cyanide	C ₂ H ₄	ethylene*		
HNC	hydrogen isocyanide	H ₂ CCCC	butatrienylidene		
HCO	formyl	CH ₃ OH	methanol		
HCO ⁺	formyl ion	CH ₃ CN	methyl cyanide		
HOC ⁺	isoformyl ion †	CH ₃ NC	methyl isocyanide		
N ₂ H ⁺	protonated nitrogen	CH ₃ SH	methyl mercaptan		
HNO	nitroxyl	NH ₂ CHO	formamide		
H ₂ O	water	HC ₃ HO	propynal		
HCS ⁺	thioformyl ion	C ₅ O	pentacarbon monoxide †		
H ₂ S	hydrogen sulfide				
OCS	carbonyl sulfide				
SO ₂	sulfur dioxide				
SiC ₂	silicon dicarbide (silacyclopropyne)*				
C ₂ S					
C ₂ O	dicarbon monoxide †				
C ₃	triatomic carbon*				

^a As of March 1991. * detected in circumstellar envelopes only. † tentative. Reported but doubtful, unconfirmed, or rejected: CO⁺, CS⁺, NaOH, NH₂CH₂COOH, CH₂CH₂O.

dense interstellar clouds. Let I_ν be the specific intensity at frequency ν , κ_ν the absorption coefficient, and ϵ_ν the volume emission rate. The equation of radiative transfer is then:

$$\frac{dI_\nu}{dl} = -\kappa_\nu I_\nu + \epsilon_\nu , \quad (12.27)$$

which in terms of the optical depth τ_ν becomes

$$d\tau_\nu = \kappa_\nu dl \quad (12.28)$$

$$\frac{dI_\nu}{d\tau_\nu} = -I_\nu + S_\nu , \quad (12.29)$$

where $S_\nu = \epsilon_\nu / \kappa_\nu$ is the **source function**. For a spectral line in a two-level system

$$\epsilon_\nu = n_2 A_{21} \frac{h\nu_0}{4\pi} \phi(\nu) , \quad (12.30)$$

where n_2 = number density per unit volume, and $\phi(\nu)$ is the normalized line profile function. The absorption coefficient includes stimulated emission (i.e. negative absorptions). So

$$\kappa_\nu = (B_{12}n_1 - B_{21}n_2) \frac{h\nu_0}{4\pi} \phi(\nu) , \quad (12.31)$$

and

$$S_\nu = \epsilon_\nu / \kappa_\nu = \frac{n_2 A_{21}}{B_{12}n_1 - B_{21}n_2} . \quad (12.32)$$

With $g_1 B_{12} = g_2 B_{21}$ and $A_{21} = B_{21} h\nu^3 / c^2$, equation (12.32) becomes

$$S_\nu = \frac{2h\nu^3}{c^2} [(n_1 g_2) / (n_2 g_1) - 1]^{-1} . \quad (12.34)$$

We can always define a relationship

$$\frac{n_2}{n_1} = \frac{g_2}{g_1} e^{-h\nu/kT_x} , \quad (12.35)$$

where T_x is the *excitation temperature* characterizing the populations in levels 1 and 2. In terms of T_x , the source function is

$$S_\nu = B_\nu(T_x) , \quad (12.36)$$

where B_ν is the familiar Planck function.

The emergent (net) intensity can also be written in terms of a **brightness temperature** T_b , or

$$I_\nu = B_\nu(T_b) , \quad (12.37)$$

so that the equation of transfer becomes

$$\frac{dI_\nu}{d\tau_\nu} = B_\nu(T_x) - B_\nu(T_b) . \quad (12.38)$$

In the Rayleigh-Jeans approximation ($h\nu \ll kT_b$)

$$kT_b \sim \frac{c^2}{2\nu^2} I_\nu \quad (12.39)$$

and

$$\frac{dT_b}{d\tau_\nu} \sim -T_b + T_x . \quad (12.40)$$

If the excitation temperature T_x is **assumed** to be uniform throughout the emitting region, the solution in the Rayleigh-Jeans limit is

$$T_b \sim T_x(1 - e^{-\tau}) + T_c e^{-\tau} , \quad (12.41)$$

where T_c is the temperature of the background radiation incident upon the far side of the emitting region and

$$\tau = \int \kappa dl \sim \frac{h\nu}{4\pi\Delta\nu} g_2 B_{21} \left(\frac{n_1}{g_1} - \frac{n_2}{g_2} \right) l \quad (12.42)$$

for a *uniform* emitting region.

Even when the Rayleigh-Jeans limit does not apply (as it does not for cold sources in the submillimeter region), one can still **define** a Rayleigh-Jeans “antenna temperature” or “radiation temperature” that is directly proportional to the specific intensity. More details are provided in the Appendix which describes the LTE line emission from the CO molecule. In practice, radio astronomical measurements are often differential measurements presented as the *difference* between an on-source signal and an off-source signal in order to remove the effects of atmospheric absorption and emission. In the case, the net Rayleigh-Jeans radiation temperature in excess of background is

$$\begin{aligned} T_A &= T_x(1 - e^{-\tau}) + T_c e^{-\tau} - T_c \\ \text{or} \quad T_A &= (T_x - T_c)(1 - e^{-\tau}) . \end{aligned} \quad (12.43)$$

Over much of the microwave, millimeter, and submillimeter parts of the spectrum, and in the absence of discrete background sources, the background radiation is typically that of the $T_c = 2.7$ K cosmic background of Big Bang fame.

Note several points:

- (1) Peak radiation temperatures as weak as $T_A = 5\text{-}10$ mK are detectable.
- (2) Detection of weak lines in emission, where “weak” means $\tau \ll 1$, requires

$$T_A \sim (T_x - 2.7)\tau > 0.01 . \quad (12.44)$$

- (3) One generally expects that molecular excitation will be at least as hot as the all pervasive $T_c = 2.7$ K background, unless there is some local, microscopic mechanism that “refrigerates” a specific molecular transition. Such an anomalous

refrigerator operates in the λ 6 cm transition of formaldehyde (H_2CO), which is widely observed in **absorption** against the cosmic background radiation.

(4) τ depends on (see e.g. (12.42)): (i) the total **column density** $N = [(\sum_i n_i)l]$ of the molecule, (ii) the **local** excitation processes such as collisions that partly govern n_1/n_2 at each point in the emitting region, and (iii) the **non-local** excitation processes, such as the absorption and stimulated emission induced by radiation produced elsewhere. In principle, one would therefore rarely expect the excitation to be uniform, but to be position-dependent and coupled in a non-linear way to the internal radiation field. If these processes are assumed to be understood, then *weak* lines with $T_A \propto \tau \propto N$ can be used to infer the *column density* of the molecule.

(5) In the limit of **large** τ (optically thick emission)

$$T_A \sim T_x - T_c, \quad (12.45)$$

and if the excitation is in LTE, i.e. $T_x \sim T_{\text{kinetic}}$, then

$$T_A \sim T_{\text{kinetic}} - T_c \quad (12.46)$$

can be used as a measure of the **kinetic temperature**.

The low rotational transitions of CO ($J=1 \rightarrow 0$, $2 \rightarrow 1$) are thermalized in many situations of interest and, due to CO's large abundance, the transitions are typically optically thick. CO is therefore widely used as a **thermometer** in interstellar clouds. Another thermometer is provided by ammonia (NH_3), or any other symmetric top molecule such as CH_3CN . As we have seen in § VIII.3, radiative transitions with $\Delta k \neq 0$ are forbidden, so that communication between ladders of differing k is governed by *collisions*. One can thus use the observed strengths of lines in different k ladders to determine the temperature. Figure 12.19 compares the temperatures for a set of sources using both the CO and NH_3 molecule. Although there are deviations in particular cases, the overall agreement is good.

How is τ related to the conditions in the emitting region? In the case of an idealized two-level system in steady state we find

$$n_1[n_c q_{12} + B_{12} J_\nu] = n_2[n_c q_{21} + A_{21} + B_{12} J_\nu], \quad (12.47)$$

where J_ν is the angle-integrated internal intensity at the location where the concentrations n_i are evaluated, n_c is a density of collision partners, and q_{ij} is a collisional (de-)excitation rate coefficient in cm^3s^{-1} . As for atoms, a **critical density** can be defined for which the collisional processes become more important than the radiative decay channels, with

$$n_{cr} = A_{21}/q_{21}. \quad (12.48)$$

The essential problem in the treatment of coupled radiative transfer and excitation lies in constructing self-consistently the emergent and internal radiation, and the location-dependent level populations that respectively determine the one and are governed by the

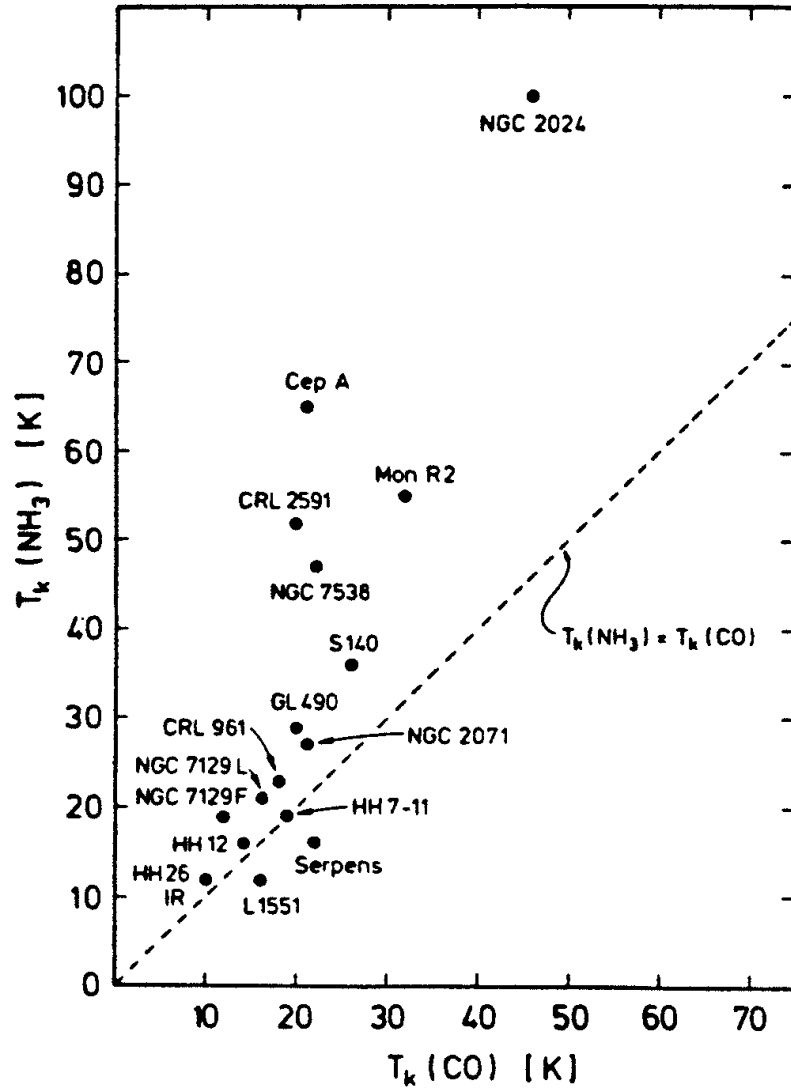


Figure 12.19– A comparison of the kinetic temperatures derived from CO and NH_3 toward dense molecular cloud cores.

other. In the general case, recall that the line profile function $\phi(\nu)$ enters into both ϵ_ν and κ_ν . This will be sensitive to the distribution of velocities within an emitting region. If a velocity gradient is sufficiently large, then line photons created within an element of doppler velocity ($v_0 \pm \delta v$) at one point in a cloud will encounter only molecules with different doppler velocities ($v' \pm \delta v'$) as they try to escape. In this case of the *large velocity gradient* (LVG), each part of a line profile corresponds to a particular location within a cloud and the emergent profile maps the dynamical structure of the object.

More realistically, clouds are probably very irregular with turbulent velocity fields. The formal radiative transfer is much more complicated. For purposes of inferring abundances, excitation, and physical conditions, however, it is often satisfactory to replace the formal solution by an approximate one at a characteristic “average” location. The

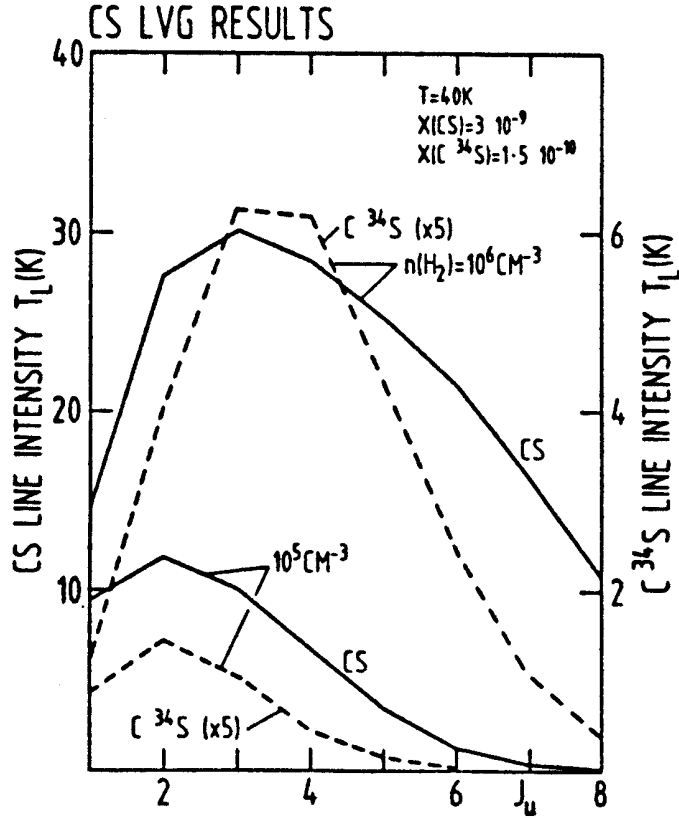


Figure 12.20– Relative populations of various J levels of CS as functions of density.

“average” internal radiation is then used to evaluate the radiative contributions to the excitation, and this mean excitation is assumed to apply to the whole cloud for the purpose of evaluating the emergent flux. This can be done through the use of a **mean escape probability** β , defined to be that fraction of the radiation produced locally that escapes.

The form of the escape probability depends on the geometry and internal structure of the source; i.e., how far the boundaries are from the point in question. For a plane parallel one-dimensional slab

$$\beta = \langle e^{-\tau} \rangle = \frac{1 - e^{-\tau}}{\tau} . \quad (12.49)$$

Thus, as $\tau \rightarrow \infty$, $\beta \rightarrow 0$; and as $\tau \rightarrow 0$, $\beta \rightarrow 1$. The spontaneous emission rate is thus effectively decreased by a factor β , so that the critical density is reduced as well, with

$$n_{cr} = A_{ul}\beta/q_{21} \sim A_{ul}/q_{21}\tau . \quad (12.50)$$

In summary, detailed comparisons of relative line strengths, combined with absolute intensities, can provide information on the column density of the molecule, and on the physical conditions such as temperature and density. We have already seen that molecules whose transitions are very optically thick are good thermometers. The best probes of the density are optically *thin* lines ($\tau \lesssim 1$) with different A-values (compare, for example, the case of atoms in § VI). Since $A \propto J^3$ for rotational levels in a diatomic molecule, a comparison of line strengths of levels with different J can give information on density. In practice, with most molecules of reasonable intensity at least one of the lines is partly optically thick, so the analysis has to take radiative transfer into account. An example is shown in Figure 12.20 for the CS molecule.

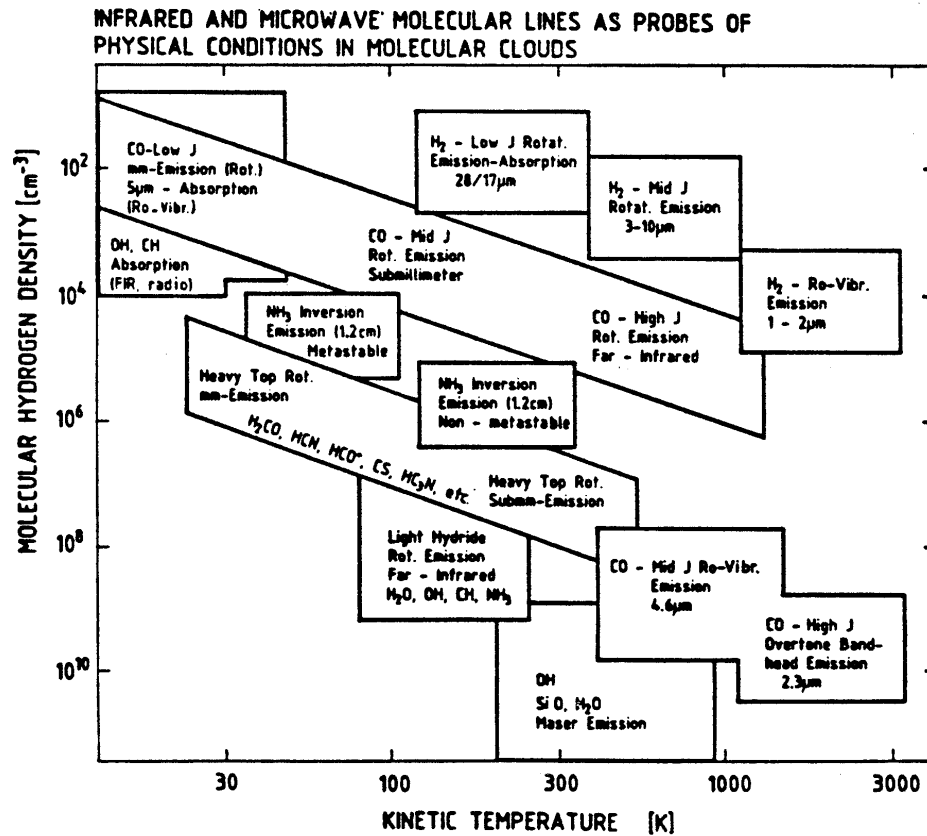


Figure 12.21– Molecular lines as probes of physical conditions in molecular clouds (and other objects as well).

It is clear that because of their different radiative and collisional properties, different molecules are sensitive to different regimes of temperature and density. For example, the critical density of the $^{12}\text{CO } J = 1 \rightarrow 0$ transition is $4 \times 10^3 \text{ cm}^{-3}$, for the $7 \rightarrow 6$ $1.6 \times 10^5 \text{ cm}^{-3}$, and for the $34 \rightarrow 33$ transition $1.6 \times 10^7 \text{ cm}^{-3}$. Thus, the higher J lines are better diagnostics of the higher density regions. At the same time, their excitation energies are higher, so that they also sample material with higher temperatures. Figure 12.21 gives a nice overview of the molecular lines that can be used to probe the physical conditions in molecular clouds.

(iii) Chemistry

The chemistry in dense clouds proceeds along the same lines as outlined for diffuse clouds, except that photodissociation is less important inside the clouds and grain mantle synthesis becomes more widespread. Thus, more complex molecules can be formed in large amounts. For more details, see for example

References

- Genzel, R. 1990, in *Chemistry in Space*, NATO ASI, ed. J.M. Greenberg.
- Herbst, E. 1988, in *Rate Coefficients in Astrochemistry*.
- Irvine, W.M. *et al.* 1987, in *Interstellar Processes*.
- van Dishoeck, E.F. 1988, in *Millimetre and Submillimetre Astronomy*.
- Walmsley, C.M. 1987, in *Physical Processes in Interstellar Clouds*.

(iv) Circumstellar Disks

The emission from interstellar dust grains and molecules serve to cool the gas in dense molecular clouds, enabling star formation to occur. Due to angular momentum constraints, the infalling material cannot directly land on the growing star, but fall onto a *circumstellar disk* that serves to transport mass inward and angular momentum outward. At the earliest phases, it is difficult to distinguish between the inner part of the collapsing envelope and a true circumstellar disk that is supported by rotation. As the envelope is exhausted, however, and the young star approaches the main sequence, the a remnant disk some few hundredths of a solar mass remains; that slow drains onto the star.

It is in such disks that planetesimals and, eventually, planets are born. Thus, it would be of great interest to compare the physical and chemical properties of circumstellar disks to the most primitive solar system materials such as comets, Kuiper Belt Objects (KBOs), and meteorites such as carbonaceous chondrites. We will examine the chemistry of comets next, and so to set the stage it is worthwhile to review what is known about disks.

The angular momentum balance dictates angular sizes of only 1-3'' at the distance of the nearest star forming clouds. In addition, circumstellar disks have large radial and angular gradients in the temperature and density profiles, and so they are difficult objects to study both observationally and theoretically. Models of the radiative energy balance in disks leads to predicted physical conditions such as those outlined in Figure 12.22.

The top and bottom of the disk is exposed to both the interstellar radiation field and photons from the young star (in addition to cosmic rays). In the outermost surface, the conditions are thus similar to what are called Photon Dominated Regions, or PDRs, while the midplane of the disk is substantially more dense than even the densest molecular cloud cores. The temperatures are also very low. Thus, the abundances of gas phase molecules in the outermost layers are low due to photodissociation, while they are low near the midplane due to the rapid depletion of gas phase molecules onto dust grains. Cosmic rays penetrate throughout the disk except for radii within a few tens of AU.

In the top row of Figure 12.22, the grey scale shows the region in which models predict the CO abundance relative to molecular hydrogen is $10^{-6} - 10^{-5}$ (dark grey) and $10^{-5} - 10^{-4}$ (light grey). The bottom panels present similar results for HCO^+ , where the numerical levels are $10^{-11} - 10^{-10}$ (dark grey) and $10^{-10} - 10^{-9}$ (light grey). The higher values are similar to those observed in molecular clouds, but apply over only a small fraction of the disk. It is thus difficult to use molecules to determine the disk mass. Such estimates therefore typically rely on the millimeter wave dust emission from disks, which at sufficiently long wavelengths is optically thin and whose intensity is directly proportional to the product of the dust mass and temperature.

Molecules do provide an excellent probe of the velocity field in cirucmstellar disks however, and can be used to examine the degree to which the assumed Keplerian velocity field is maintained. In large beams that include the entire disk, the shape of the millimeter-wave emission lines can used to estimate the extent of the disk, provided the inclination angle is known. When the disk is oriented in the plane of the sky, or “face on”, there is no doppler component of the orbital velocity along the line-of-sight, and so a single-peaked line is obtained. For an inclined disk and lines that are optically thick, a double-peaked line is obtained whose peak separations and width are sensitive functions of the mass of the

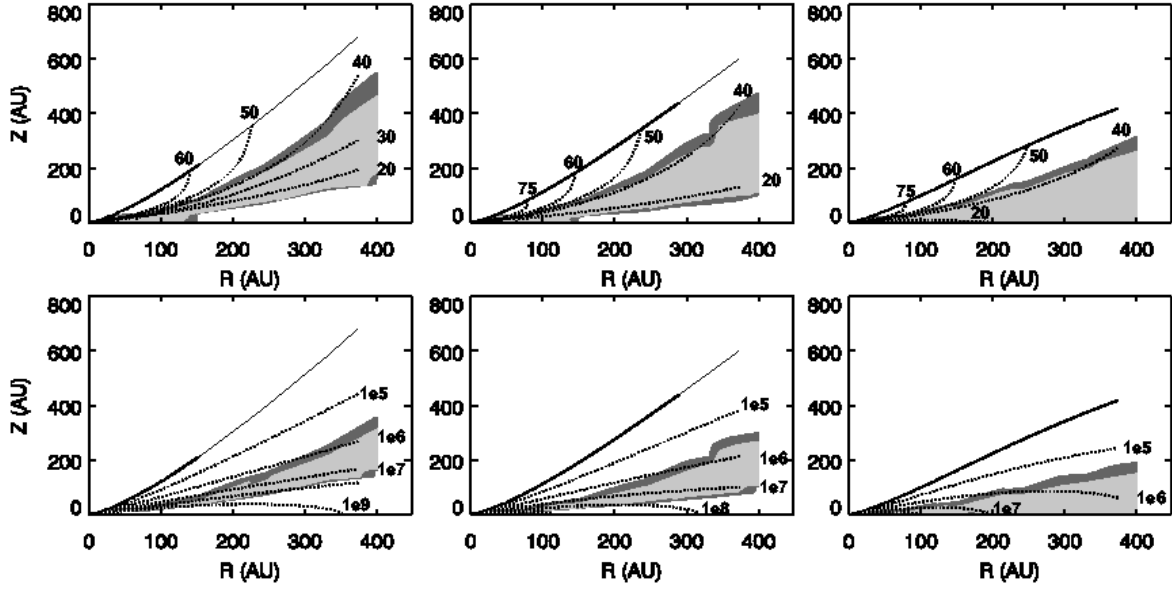


Figure 12.22– The distributions of temperature (K) and density ($n(\text{H}_2) \text{ cm}^{-3}$) from model circumstellar accretion disks. The viscosity parameter is $\alpha = 0.1$, and the mass accretion rates drop from 10^{-7} to 10^{-8} to $10^{-9} M_{\odot} \text{ yr}^{-1}$ from left to right. The upper boundary layer of the disk is defined as the location where the density drops to $1.4 \times 10^4 \text{ cm}^{-3}$ at a temperature of 50 K.

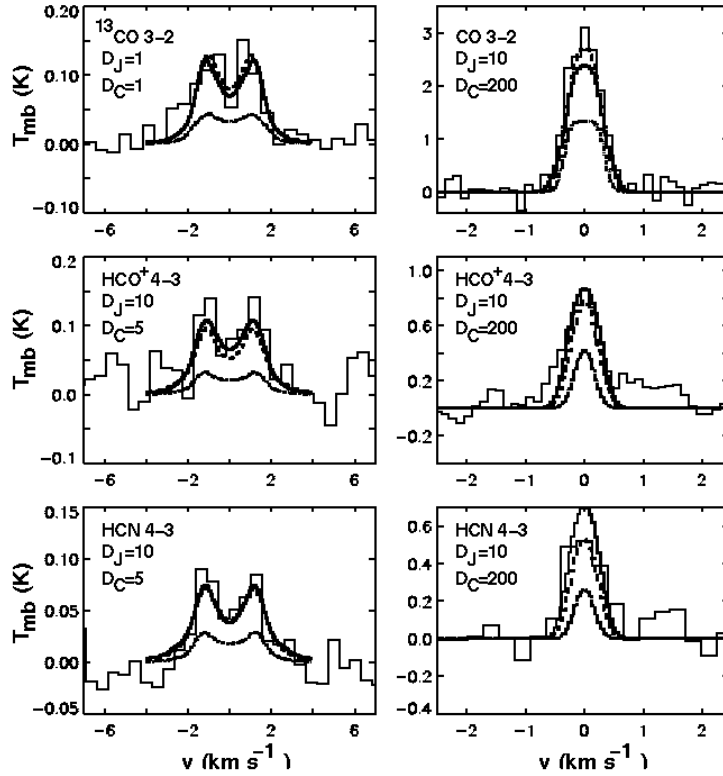


Figure 12.23– Observed millimeter-wave emission lines from two circumstellar disks; LkCa 15 is inclined while TW Hydra is nearly face on. The lines depict the results of LVG radiative transfer models of the disks for a variety of abundances influenced by depletion onto grains; the depletion values are listed in the separate panels.

central star, the disk radius, and the disk inclination. For spatially resolved observations, such as those possible with millimeter-wave interferometers, the observed patterns can be used to fit these parameters to a high degree of precision (c.f. Figure 12.24). Once these physical characteristics are established, reasonably accurate molecular abundances in the vertical zones accessible to observation can be obtained.

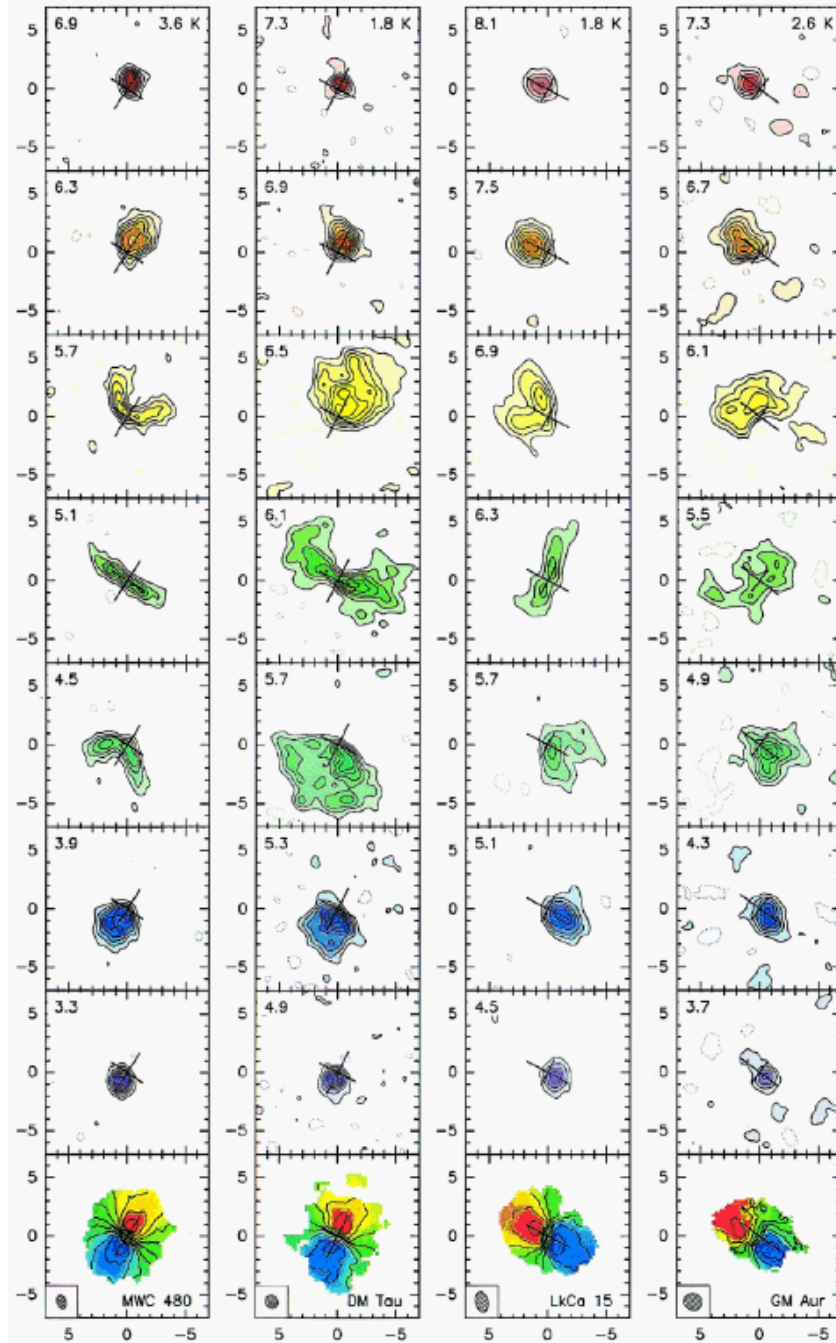


Figure 12.24– Plateau de Bure interferometric “channel maps” of the CO 2→1 emission from the circumstellar disks surrounding the Herbig Ae star MWC 480 and the T Tauri stars DM Tau, LkCa 15, and GM Aur. The v_{LSR} of the channels are at the upper left of each panel, the velocity maps and synthesized beams are shown in the lowermost row.

4. Comets

(a) Introduction

Comets are small bodies of the solar system a few kilometers in size that move in elliptical orbits about the Sun. Comets spend most of their time orbiting at distances of $\sim 50,000$ AU from the Sun in the so-called **Oort cloud**. Perturbations either by collisions with another object, or by gravitational tugs of a nearby star, can cause a comet to deviate from its normal path so that it falls inward toward the Sun. For most of its lifetime, a comet is just a frozen chunk of icy material, consisting of small particles like gravel or larger rocks that are embedded in frozen gases. Whipple, who first suggested this model in the 1950's, appropriately called comets "dirty snowballs." Thus, as the comet passes through the outer part of the solar system, it is not easily visible from Earth.

As the comet approaches the Sun, however, it warms up and the volatile gases begin to escape. A spherical cloud of gas called the *coma* develops around the nucleus when it is closer than about 5-10 AU from the Sun (from *κομητης* = long-haired; coma = hair). This neutral coma may be as large as 10^5 km, and the gas moves nearly radially outward at speeds of about 1 km s^{-1} . In contrast with planetary atmospheres, the coma is **not** gravitationally bound to the central body. The difference with asteroids is, of course, that the latter are essentially rock-like and possess no atmosphere.

The solar radiation pressure and the solar wind force some of the dust and gas from the coma to flow away from the Sun, forming a *tail* which may be as long as 10^8 km. There are often two distinct tails: the plasma or *ion-tail* and the *dust tail*. The ion tail contains molecules from the coma that have been ionized by the solar wind, such as CO^+ , N_2^+ , ... This tail points almost exactly straight away from the Sun at all times. The *dust* tail usually takes a curving shape, as the dust particles inherit the comet's velocity and are pushed away from the Sun by radiation pressure.

Many of these "new" comets falling in from the Oort cloud follow a highly elongated orbit with a period of millions of years, making only a brief passage near the Sun. These are so-called **long-period** comets. In some cases, however, interactions with the gravitational field of a planet, e.g. Jupiter, may cause the comet to slow down and drop into a smaller orbit with a shorter period. It then becomes one of the **short-period** comets. An example of a short-period comet is Encke, which appears every 3.3 years. If a comet makes several close passages to the Sun, it will eventually sublimate all of its volatile gases, break up, and leave behind nothing but dusty debris. This debris can be seen each year in a number of *meteor showers* (i.e. the Perseids, the Leonids, ...).

The study of comets is of interest because they contain the most primitive solar system material. Although the birth-site of comets is still subject to considerable debate, it is certainly no closer than 20-30 AU to the Sun, and may be much larger. Thus, comets have undergone the least processing of material in the solar nebula, and may therefore be our best probes of the physical and chemical conditions in the outer regions of the solar nebula during the period of planet formation. The volatile inventory of cometary nuclei in particular can be used to decide whether comets are the product of a condensation sequence similar to that invoked to explain the compositions of the planets and asteroids, or if the cometary material is compositionally similar to that of the interstellar molecular cloud from which the solar system formed.

Observationally, the volatile inventory is not easy to determine, since the composition of the icy nucleus is not directly detected. Rather, the gaseous and solid components of the extended coma are observed, and it is from the spectral and spatial information about the coma, together with photochemical modeling, that the composition of the cometary ices must be inferred. The recent apparitions of the comets Hyukutake and, especially, Hale-Bopp have led to a number of new discoveries with the improved astronomical instrumentation available, and so we will first cover what is generally known about comets before turning to a summary of recent research.

(b) Observations

(i) Optical and UV Studies

Cometary comae have been studied in detail at visible wavelengths (3000 – 8000 Å) since the 1930's. Figure 12.25 shows a low resolution optical spectrum of Comet Halley. The dominant emission is provided by the C_2 d $^3\Pi_g - a^3\Pi_u$ Swan system at 5100 Å and the CN B $^2\Sigma^+ - X^2\Sigma^+$ violet system at 3870 Å (not shown in Figure 12.25). For the C_2 Swan system, several band **sequences** are seen, which have common values of Δv . Thus, at 5100 Å, the emission consists of a superposition of bands with $\Delta v = 0$. The (0,0) band is the strongest, but the (1,1), (2,2), ..., (5,5),... bands still contribute significantly.

The $\Delta v = -1$ sequence, consisting of the $(v', v'') = (0,1), (1,2), \dots$ bands, occurs at longer wavelengths around 5500 Å, whereas the $\Delta v = 1$ sequence, containing the (1,0), (2,1), ... bands, is seen around 4600 Å. Figure 12.26 shows the observed spectrum in the region of the (0,0) band at much higher resolution. Since the equilibrium internuclear distance in the upper d $^3\Pi_g$ state is *less* than that in the $a^3\Pi_u$ state, the band is shaded toward the **blue**, i.e., both the P and R lines appear at wavelengths shortward of the band head. See Figure 12.26 for a quantitative example.

As noted before, C_2 has a complicated energy level structure. Figure 12.27 illustrates some of the potential energy curves for the molecule (repulsive curves have been omitted for clarity), and Table 12.4 summarizes the nomenclature for several of the observed bands. Apart from the Swan system, the Phillips A $^1\Pi_u - X^1\Sigma_g^+$ and the Mulliken D $^1\Sigma_u^+ - X^1\Sigma_g^+$ systems have also been detected in comets. Other molecules detected at visible wavelengths include CH, C_3 , CN, NH, NH_2 , OH, and HCO. In the ion tail, CO^+ , H_2O^+ , CO_2^+ , N_2^+ , CH^+ , CN^+ , OH^+ , and H_2S^+ have been seen. These emissions result from *resonance fluorescence* of the solar radiation.

With the advent of the International Ultraviolet Explorer (IUE) satellite in January 1978, it has also become possible to observe comets at ultraviolet (UV) wavelengths. Nearly two dozen comets have since been observed. Since many atoms and molecules have strong electronic transitions at UV wavelengths, the UV observations have greatly added to our knowledge of the composition of cometary comae – and thereby cometary ices. An example of the UV spectrum from comet Bradfield (1979 X) was shown in the introduction. Figure 12.28 shows the UV spectrum of comet Halley at the time of closest approach to the Sun. Table 12.5 summarizes the UV wavelengths at which the various species can be observed. Note that the important molecules CO and H_2 can only be observed at these wavelengths. Thus absence of an emission feature of H_2 at 1608 Å (corresponding to the Lyman B – X transitions) puts an upper limit on its abundance.

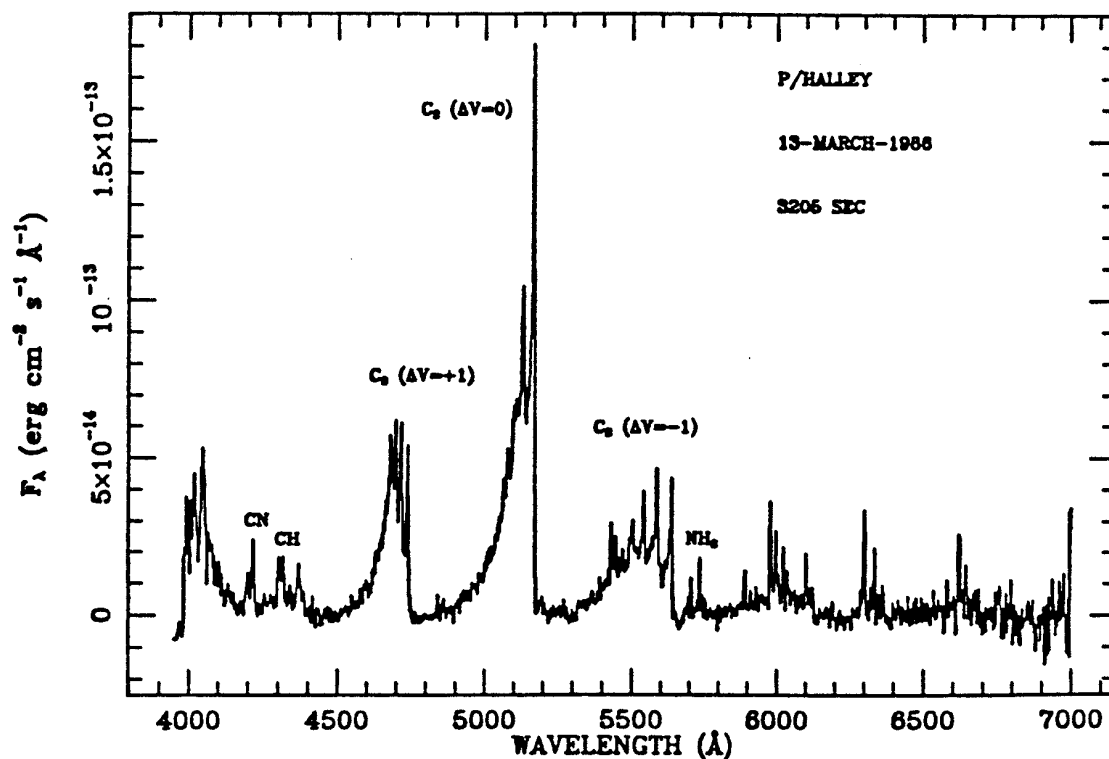


Figure 12.25– Visible spectrum of comet Halley at low spectral resolution.

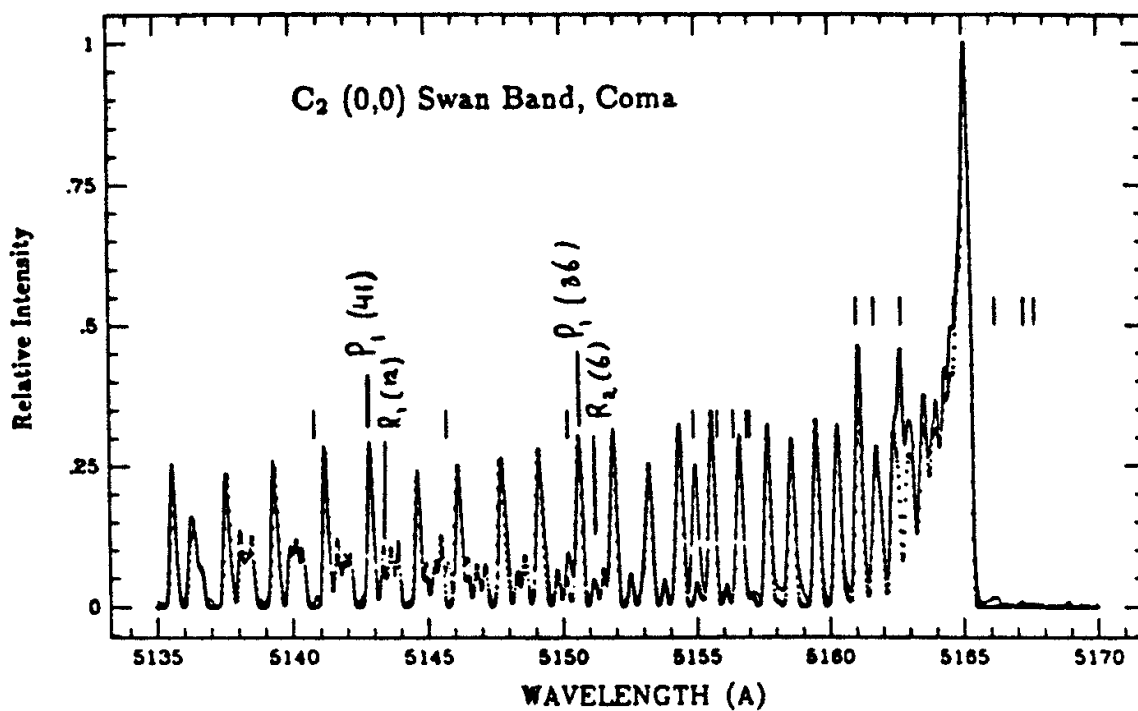


Figure 12.26– High resolution spectrum of the C_2 (0,0) Swan band in comet Halley.

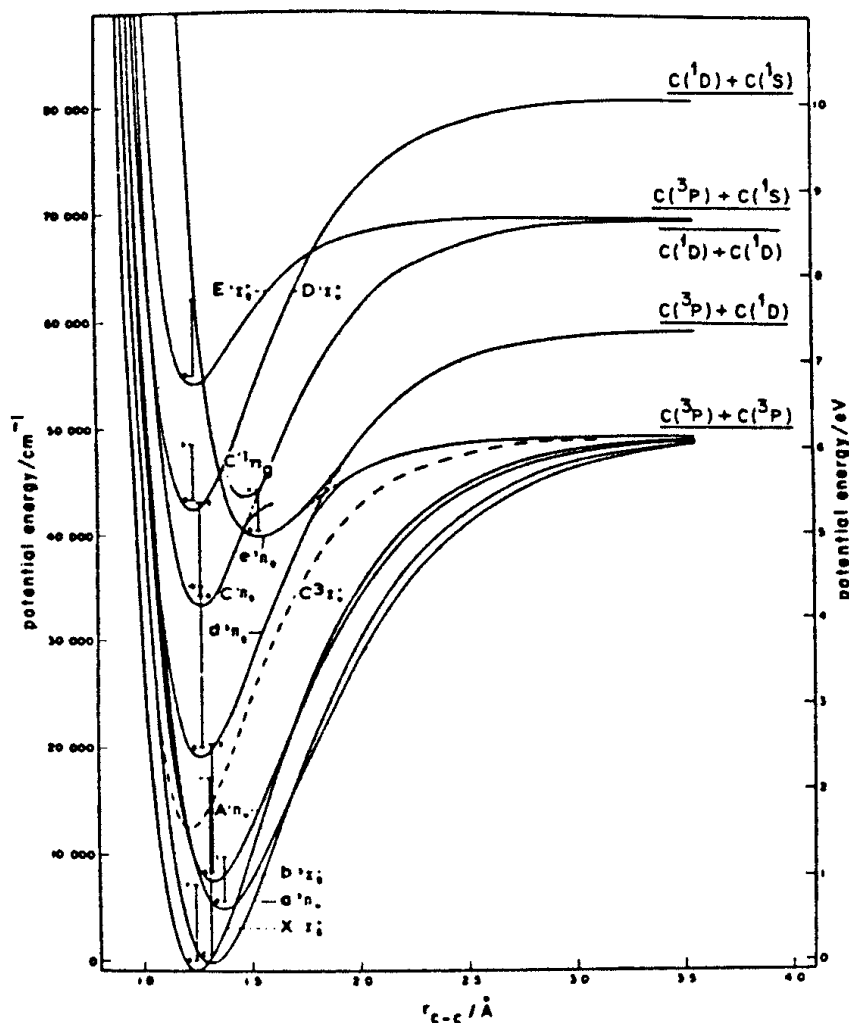


Figure 12.27– Potential energy curves for the ground and several excited states of C_2 (Balik and Ramsey 1963, *Ap. J.* 84, 137).

Table 12.4– Electronic Transitions in C_2

Transition	Names associated	Spectral region/nm	Source of spectrum
$b^1\Sigma_g^- \rightarrow a^3\Pi_u$	Ballik–Ramsay	2700–1100	King furnace
$A^1\Pi_g \leftarrow X^1\Sigma_g^+$	Phillips	1549– 672	Discharges
$d^3\Pi_g \leftarrow a^3\Pi_u$	Swan	785– 340	Numerous, including carbon arc
$C^1\Pi_g \rightarrow A^1\Pi_u$	Deslandres–d’Azambuja	411– 339	Discharges, flames
$e^1\Pi_g \rightarrow a^3\Pi_u$	Fox–Herzberg	329– 237	Discharges
$D^1\Sigma_g^+ \leftarrow X^1\Sigma_g^+$	Mulliken	242– 231	Discharges, flames
$E^1\Sigma_g^+ \rightarrow A^1\Pi_u$	Freymark	222– 207	Discharge in acetylene
$P^1\Sigma_g^- \leftarrow a^3\Pi_u$	—	143– 137	Flash photolysis of mixture of a hydrocarbon and an inert gas
$g^3\Delta_g \leftarrow a^3\Pi_u$	—	140– 137	
$F^1\Pi_u \leftarrow X^1\Sigma_g^+$	—	135– 131	

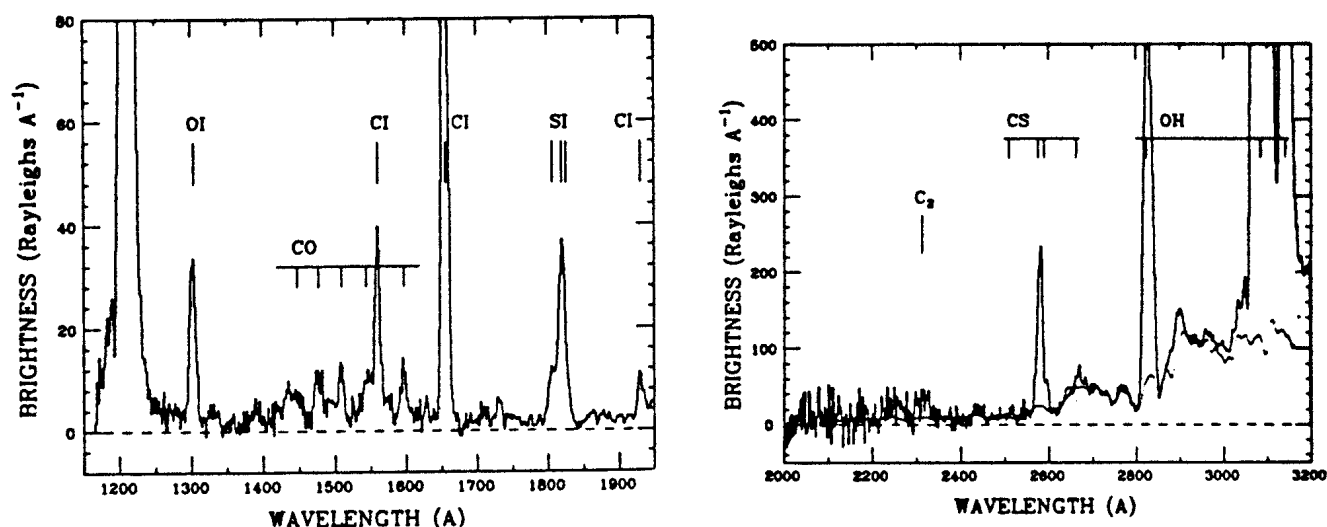


Figure 12.28– The UV spectrum of comet Halley.

Table 12.5– Cometary UV Emission Features

Observed Species	Wavelength (Å)	Possible Species	Wavelength (Å)
H I (Lyman- α)	1216	H ₂	1608
O I	1304	NO	2150
C II	1335	CO ₂	2000 – 2200
C I	1561, 1657	SO	2635
S I	1813	SH	3261
C I (¹ D)	1931		
CO	1475 – 1600		
C ₂	2313		
CS	2576		
S ₂	2850 – 3050		
OH ⁺	3085		
CO ⁺	2188		
CO ₂	2890		

The UV wavelength region is particularly useful for detecting atomic sulfur and sulfur-containing molecules. Both S I and CS are common features of cometary spectra. The close approach to Earth of comet IRAS Araki-Alcock (1983 VII) enabled the IUE discovery of S₂, which has not yet been detected in any other comet, or any other astronomical source. The molecules SH and SO, although searched for, have not yet been detected in cometary spectra at optical/UV wavelengths. Atoms detected in these spectral regions include H, C, N, O, S, Na, Al, Fe, Ni, K, Ca, Cr, Mn, Cr, Co, V, and C⁺/Ca⁺ (in the ion tail).

(ii) Infrared and Radio/(Sub)millimeter-wave Observations

Searches for molecules in comets via their vibrational (infrared wavelengths) and rotational (radio and millimeter wavelengths) degrees of freedom were, until recently, largely unsuccessful due to a combination of factors. First, the relatively small column densities of the species of interest compared with those that are found in molecular clouds result in spectral line features that are often relatively weak unless the comet is very close or very large. Second, the detector and spectrograph technologies in these areas have been advancing rapidly, such that the critical sensitivity thresholds for comets were reached only within the last decade. Finally, the recent apparitions of comets Halley, Hyukutake, and Hale-Bopp have provided extraordinary observational opportunities. Halley was the first comet investigated by detailed *in situ* techniques; Hyukutake, while small, passed very near the Earth (~ 0.1 AU); and Hale-Bopp was among the largest comets to pass within the inner solar system for the past several thousand years (the time scale of recorded human observations of the sky). In the past, it was only large dipole moment species such as HCN, H_2CO , and CH_3CN that were amenable to radio observations, now a host of species can be studied. At centimeter wavelengths, it is the inversion transitions of NH_3 and the 18 cm spin-rotation transitions of OH that are most widely detected.

Infrared observations of important molecules such as H_2O and CO_2 are potentially very useful, but are extremely difficult because of the interference by the Earth's atmosphere. Nevertheless, H_2O was unambiguously identified for the first time in comet Halley through airborne infrared observations. Figure 12.29 shows the observed spectrum. With the launch of ISO in the 1990's, studies free of the atmospheric interference became possible, with CO_2 being detected, in comet Hale-Bopp, for the first time (see Figure 12.30). For both Halley and Hale-Bopp, the ortho-para spin temperature of the infrared water measurements is approximately 25 K. A similar conclusion is reached from the abundances of volatiles such as N_2 , CH_4 , and C_2H_6 . Mapping of the IR spectral features reveals both compact sources of molecules as well as a much more extended source, typically assumed to be sublimation or photochemical processing of icy mantles on dust grains.

Like the optical/UV studies outlined above, the near-IR emission is produced by resonance fluorescence. Thus, the distance dependence of the emission is extremely steep, $\sim r^{-4}$ due to the round trip nature of the excitation/decay. Millimeter-wave emission lines from comets, like those from planetary atmospheres, are caused by collisions. Thus, the intensities of these lines scale like r^{-2} (for constant outgassing rates). In Hale-Bopp, this shallower distance dependence enabled observations of the coma to distances as large as 7 AU. As Figure 12.31 shows, these measurements reveal a clear transition from CO-dominated outgassing at large distances to the expected water-dominated outgassing near perihelion. Hale-Bopp was also sufficiently bright that millimeter-wave interferometric techniques could be applied for the first time; resulting in high spatial resolution images that trace both the direct nuclear outgassing as well as that from icy grains lifted by jetting activity. An example of this work is shown for the DCN molecule in Figure 12.32.

Table 12.6 summarizes all of the cometary volatiles observed to date at infrared and (sub)millimeter wavelengths. What do these observations tell us?

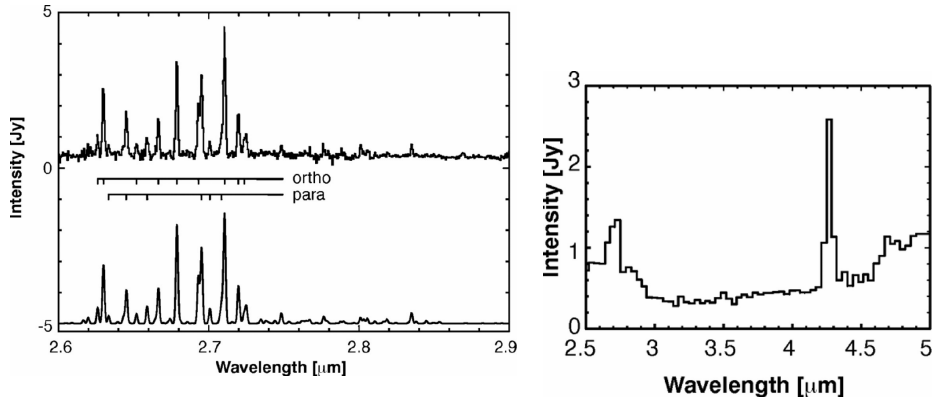


Figure 12.30– (Left) ISO PHT-S 2.5-5 μm spectrum of Hale-Bopp on 27 September 1996, at a spectral resolution of ~ 90 . H_2O and CO_2 bands are easily visible (CO is at $4.65 \mu\text{m}$). (Right) ISO SWS spectra of water vapor in the coma of Hale-Bopp. The spectral resolution is ~ 1500 . The best fit yields $T_{\text{ROT}} = 28.5 \text{ K}$ and $\text{OPR} = 2.45$.

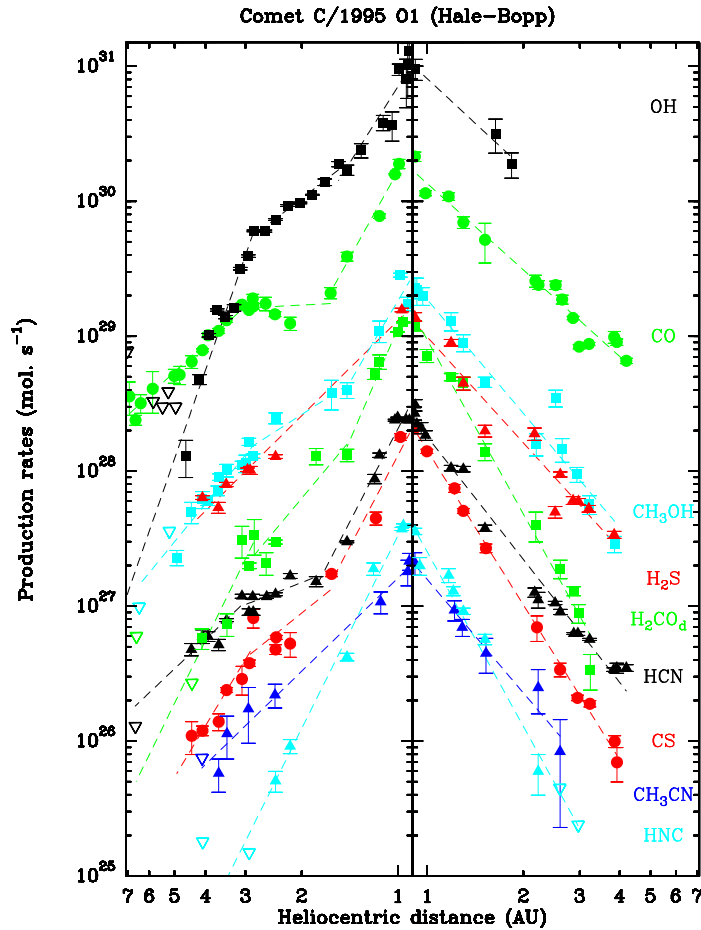


Figure 12.31– Comet Hale-Bopp production rates versus heliocentric distance. Approach is to the left. Note the switch from CO to H_2O outgassing near 3 AU.

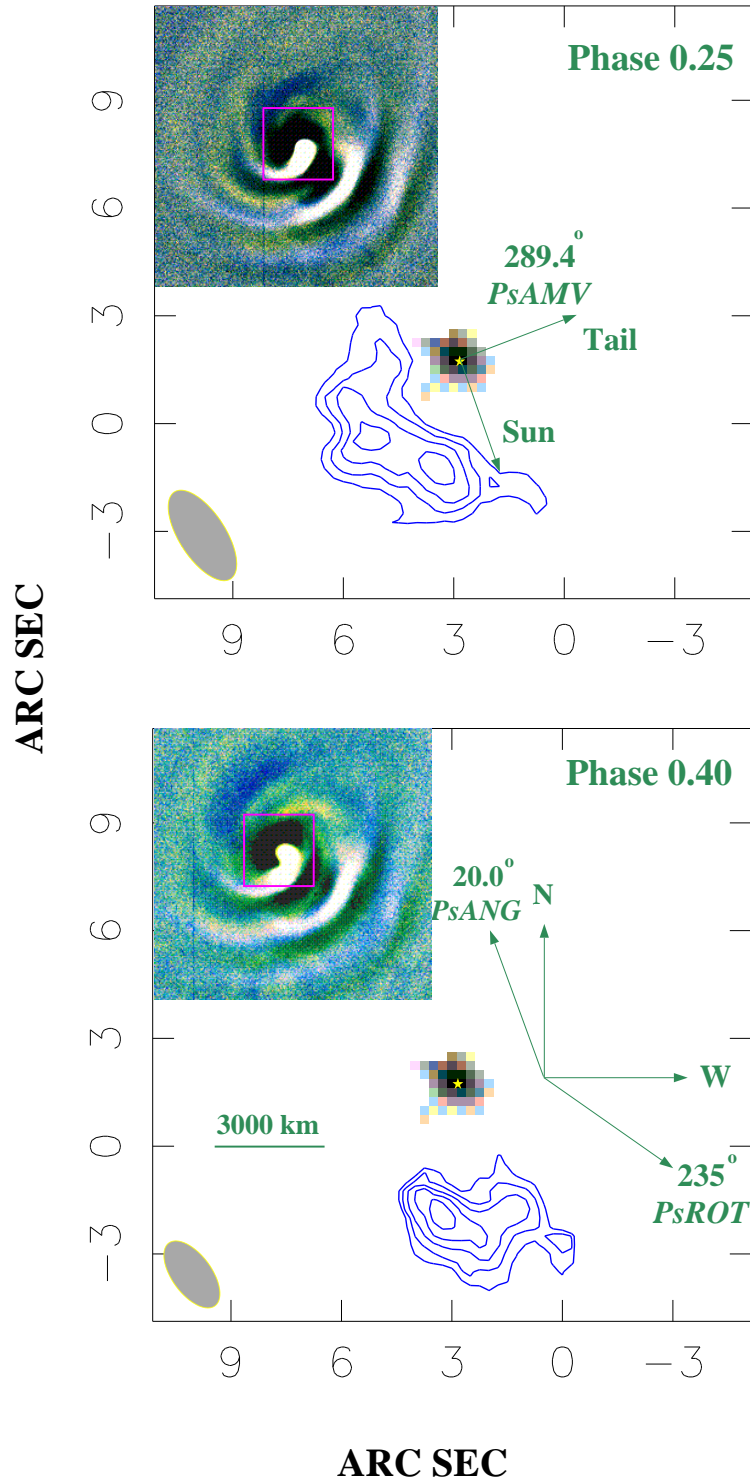


Figure 12.32– OVRO aperture synthesis images of Hale-Bopp. The grey scale presents the dust continuum emission, the contours the DCN 3→2 emission at 217 GHz. The time between the two plots is approximately two hours. The inset depicts a highly stretched optical image of Hale-Bopp, illustrating the jet activity and orientation.

Table 12.6– Cometary Volatiles Observed in the IR and MM-Wave Regions

Molecule	[]/[HCN] (%)	[]/[H ₂ O] (%)	Molecule	[]/[HCN] (%)	[]/[H ₂ O] (%)
H ₂ O	40000	100	NH ₃		0.7
CO	9000	23	HCN	100	0.25
CO ₂		6	HNCO	39	0.10
			HNC	14	0.035
CH ₄		0.6	CH ₃ CN	7.9	0.020
C ₂ H ₂		0.1	HC ₃ N	7.7	0.019
C ₂ H ₆		0.3			
			H ₂ S	590	1.5
CH ₃ OH	960	2.4	SO	111	0.28
H ₂ CO	450	1.1	CS ₂	67	0.17
HCOOH	33	0.08	SO ₂	85	0.21
HCOOCH ₃	24–43	0.06–0.11	OCS	148	0.38
NH ₂ CHO	4.0–8.0	0.01–0.02	H ₂ CS		0.02

(c) Models

The basic models for the cometary nucleus and coma were developed already in the 1950's by Whipple and Haser, respectively. Whipple's original "icy-conglomerate" model contained nearly equal amounts of H₂O, CH₄, NH₃, and CO₂. The recent apparitions have enabled the first set of accurate abundances (or at least limits on them!) to be assembled, as Table 12.6 shows. This is largely due to spacecraft flybys. H₂O is by far the most important constituent. Haser developed in 1957 a very simple model to account for the observed abundances of the radicals in cometary atmospheres. He recognized that as the so-called **parent** molecules H₂O, CH₄, ... are sublimated from the nucleus when the comet approaches the Sun, they can be photodissociated by the solar radiation. Thus, they flow outward from the nucleus only over a characteristic *scale length* determined by the photodissociation rate. The resulting **daughter** molecules are distributed over larger distances, with a scale length determined by their photodissociation rate. This simple model has been improved upon by taking the kinematics of the dissociation process into account, and by treating the chemistry in more detail, but the basic picture remains valid. Figures 12.33 and 12.34 show the variations of the densities and column densities of a number of species as functions of distance from the cometary nucleus. Photodissociation is the primary chemical process. Ion-molecule and neutral-neutral reactions are important only in the inner 300 km of the coma, where the densities are high.

Since most of the proposed parent molecules cannot be directly observed, or only with great difficulty, from the Earth at optical wavelengths, their abundances must be inferred from detailed modeling of the measured abundances and distributions of the various daughter and granddaughter molecules. The observed abundances of C₂ and C₃ clearly suggest that more complicated parent molecules, such as C₂H₂, must be present in the ices. Very complex hydrocarbon molecules, such as polymerized formaldehyde (POM) or HCON particles, are also probably present in the cometary nucleus. Observations in the IR and (sub)millimeter-wave probe the inner coma and have provided the first robust look at the parent molecules in cometary ices.

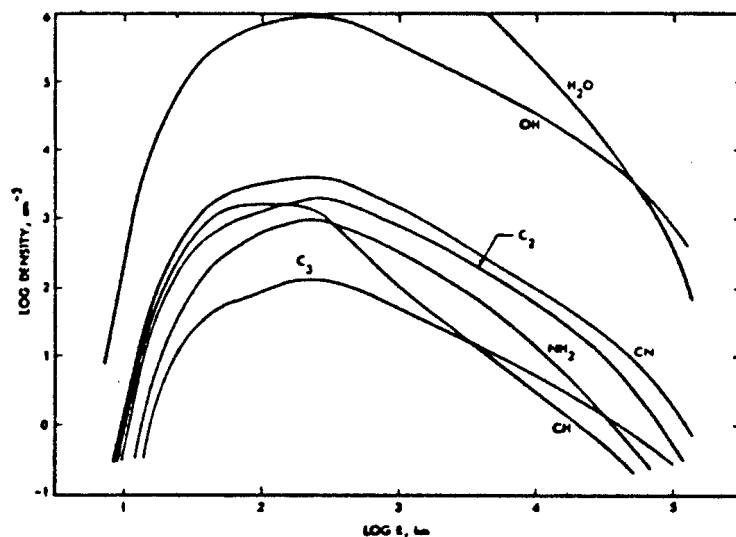


Figure 12.33– Variation of the abundances of several neutral species through the coma for a “standard” kinetic model.

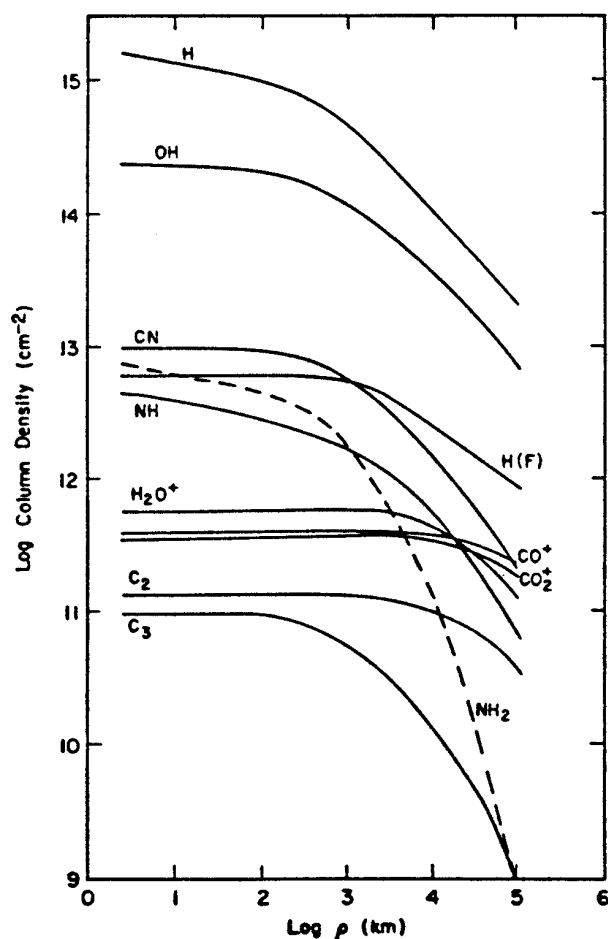


Figure 12.34– Model results for column densities of selected species plotted as a function of projected distance on the sky. Thermal hydrogen is indicated by H, fast photochemical hydrogen by H(F).

Table 12.7– A Comparison of Interstellar Ice and Comet Volatiles

Species	NGC 7538 IRS 9	W 33A	Hale–Bopp
H ₂ O	100	100	100
CO (total)	10	3	23
CO (polar)	3	2	
CO (apolar)	7	1	
CO ₂	16	4	6
CO ₂ (polar)	1	1	
CO ₂ (annealed)	3	2	
CH ₃ OH	9	10	2
H ₂ CO	3	2	1
HCOOH	2	0.5	0.1
NH ₃	10	4	0.7
CH ₄	1	0.4	0.6
OCS	0.1	0.05	0.4
‘XCN’	0.8	1	

^a Relative to H₂O=100. Adopted H₂O column densities are 10¹⁹ and 4 × 10¹⁹ cm^{−2} for NGC 7538 IRS 9 and W 33A, respectively.

References: Interstellar ices: H₂O, H₂CO, HCOOH: Keane et al. (2000); CO: Tielens et al. (1991); CO₂: Gerakines et al. (1999); CH₃OH: Allamandola et al. (1992); NH₃: Lacy et al. (1998); CH₄: Boogert et al. (1998); OCS: Palumbo et al. (1997); ‘XCN’: Pendleton et al. (1999). Comet Hale Bopp: Bockelée-Morvan et al. (2000).

Although more than two dozen comets have been studied, only for a few comets have abundances been reliably determined. It is not yet known how characteristic these abundances are for other classes of comets (e.g. long-period versus short-period comets). It is clear from the observations that the ratio of dust-to-gas is highly variable, and is probably correlated with the number of times the comet has been close to the Sun. On the other hand, the ratios of the major gas emitters, such as the C₂/CN ratio, are remarkably consistent from comet to comet. It is not yet clear whether the derived abundances of the parent molecules in comets resemble more those found in interstellar clouds, or those expected in the outer solar nebula, because in both environments a mix of oxidized and reduced species is expected. Nevertheless, it is clear that future cometary missions, combined with ground-based, airborne, and space-based observations, can provide a more quantitative understanding of the link between comet composition, cometary formation environments, and the star/planet formation process.

References

- Huebner, W.F. 1984, in *Molecular Astrophysics*, p. 311.
Feldman, P.D. 1987, in *Astrochemistry*, IAU Symposium 120.
Weaver, H.A. 1988, in *Highlights of Astronomy* Vol. 8, p. 387.
Festou, M.C. et al. 1993, *Astrophys. Rev.* **5**, 37.
Biver, N. et al. 1997, *Science* **275**, 1915.
DiSanti, M.A. et al. 2001, *Icarus* **153**, 361.